RMetS
Royal Meteorological Society

Solar signals in CMIP-5 simulations: the ozone response

L. L. Hood,[a]* S. Misios,[b] D. M. Mitchell,[c] E. Rozanov,[d,e] L. J. Gray,[c,f] K. Tourpali,[b] K. Matthes,[g,h] H. Schmidt,[i] G. Chiodo,[j,k] R. Thiéblemont,[g] D. Shindell[l] and A. Krivolutsky[m]

[a]*Lunar and Planetary Laboratory, University of Arizona, Tucson, USA*
[b]*Laboratory of Atmospheric Physics, Aristotle University of Thessaloniki, Greece*
[c]*Atmospheric, Oceanic and Planetary Physics, University of Oxford, UK*
[d]*Physikalisch-Meteorologisches Observatorium, World Radiation Center, Davos Dorf, Switzerland*
[e]*Institute for Atmospheric and Climate Science, ETH, Zurich, Switzerland*
[f]*NERC, National Centre for Atmospheric Science (NCAS), Leeds, UK*
[g]*GEOMAR Helmholtz Centre for Ocean Research, Kiel, Germany*
[h]*Christian-Albrechts Universität zu Kiel, Germany*
[i]*Max Planck Institute for Meteorology, Hamburg, Germany*
[j]*Departamento Fisica de la Tierra II, Universidad Complutense de Madrid, Spain*
[k]*Applied Physics and Applied Mathematics, Columbia University, New York, NY, USA*
[l]*Nicholas School of the Environment, Duke University, Durham, NC, USA*
[m]*Laboratory for Atmospheric Chemistry and Dynamics, Central Aerological Observatory, Moscow, Russia*

*Correspondence to: L. L. Hood, LPL, University of Arizona, 1629 E. University Boulevard, Tucson, AZ 85721, USA.
E-mail: lon@lpl.arizona.edu

A multiple linear regression statistical method is applied to model data taken from the Coupled Model Intercomparison Project, phase 5 (CMIP-5) to estimate the 11-year solar cycle responses of stratospheric ozone, temperature, and zonal wind during the 1979–2005 period. The analysis is limited to the six CMIP-5 models which resolve the stratosphere (high-top models) and which include interactive ozone chemistry. All simulations assumed a conservative 11-year solar spectral irradiance (SSI) variation based on the Naval Research Laboratory model. These model responses are then compared to corresponding observational estimates derived from two independent satellite ozone profile datasets and from ERA-Interim reanalysis meteorological data. The models exhibit a range of 11-year responses with three models (CESM1-WACCM, MIROC-ESM-CHEM and MRI-ESM1) yielding substantial solar-induced ozone changes in the upper stratosphere which compare favourably with available observations. The remaining three models do not, apparently because of differences in the details of their radiation and photolysis rate codes. During winter in both hemispheres, the three models with stronger upper-stratospheric ozone responses produce relatively strong latitudinal gradients of ozone and temperature in the upper stratosphere which are associated with accelerations of the polar night jet under solar maximum conditions. This behaviour is similar to that found in the satellite ozone and ERA-Interim data, except that the latitudinal gradients tend to occur at somewhat higher latitudes in the models. The sharp ozone gradients are dynamical in origin and assist in radiatively enhancing the temperature gradients, leading to a stronger zonal wind response. These results suggest that simulation of a realistic solar-induced variation of upper-stratospheric ozone, temperature and zonal wind in winter is possible for at least some coupled climate models even if a conservative SSI variation is adopted.

Key Words: SolarMIP; solar; stratosphere; ozone; CMIP-5; natural variability

Received 5 December 2014; Revised 14 March 2015; Accepted 18 March 2015; Published online in Wiley Online Library 22 April 2015

1. Introduction

As reviewed by Mitchell *et al.* (2014a) (hereafter referred to as Article 1), the stratosphere containing the ozone layer represents a key link through which solar variability can produce perturbations of tropospheric circulation. Solar influences on surface climate can, in principle, be due either to solar irradiance variations or changes in corpuscular radiation (energetic charged particles), or

both (e.g. section 4 of the review by Gray *et al.*, 2010). Influences of solar irradiance variability can be further divided into a so-called 'bottom-up' category, involving direct penetration of solar radiation at wavelengths greater than about 300 nm to the lower troposphere, and a 'top-down' category, involving effects of solar ultraviolet (UV) radiation on the upper atmosphere with indirect dynamical effects at lower levels. Because of the important role of ozone, which is mainly produced by solar UV radiation, in radiatively heating the stratosphere and because solar UV variability is relatively large (up to ∼6% near 200 nm over an 11-year cycle compared to ∼0.1% at wavelengths >300 nm), top-down solar irradiance forcing is believed to be a non-negligible component of solar-induced climate variability (Haigh, 1994, 2003; Kodera and Kuroda, 2002; Matthes *et al.*, 2006; Meehl *et al.*, 2009; Gray *et al.*, 2013; Hood *et al.*, 2013).

There are a number of sources of uncertainty in designing a general circulation model (GCM) that is able to simulate the observed top-down component of solar irradiance-induced climate change. These include uncertainties in solar spectral irradiance (SSI) variability itself, uncertainties in observational estimates for the solar-induced stratospheric and surface climate response, and uncertainties in the model formulation (section 2.2).

The nature and magnitude of SSI variability has been a topic of increased attention during the last decade. Due to a lack of direct, long-term measurements of SSI, proxy-based models have previously been developed by several groups using indirect measurements such as sunspot area, the solar 10.7 cm radio flux (F10.7), and the solar Mg II core-to-wing ratio (review by Ermolli *et al.*, 2013). These SSI models have been extensively employed in climate model simulations. For example, the SSI model developed at the US Naval Research Laboratory (NRL SSI; Lean *et al.*, 1995; Lean, 2000; Wang *et al.*, 2005) has been adopted for use by most models in the most recent Coupled Model Intercomparison Project (CMIP-5; Taylor *et al.*, 2012).

New direct satellite-based measurements of SSI began to be obtained in 2003 by the SOlar Radiation and Climate Experiment (SORCE; e.g. Harder *et al.*, 2009). As reviewed by Ermolli *et al.* (2013), the SORCE measurements differ in major ways from the proxy-based models and some of these differences may be a consequence of instrument degradation with time (e.g. Lean and DeLand, 2012). In particular, a large SSI decrease in the 200–320 nm range was measured by SORCE during the decline of solar cycle 23 that was four to six times larger than estimated by proxy-based models. Ermolli *et al.* (2013) conclude that a lower limit on the magnitude of the SSI solar cycle variation is represented by the NRL SSI model while the SORCE measurements may represent an upper limit. However, results of recent efforts to account for and correct instrument degradation effects in the SORCE SSI data (e.g. Woods, 2012) suggest that the measured upper limit will be revised downward considerably.

This is the second in a series of analyses performed as part of the SPARC SOLARIS-HEPPA Solar Model Intercomparison Project (SolarMIP). In Article 1, multiple linear regression (MLR) was applied to assess the 11-year solar cycle component of both stratospheric and surface climate variability in the full suite of more than 30 models that contributed to the CMIP-5 comparison study. The analysis focused on the 13 models which resolve the stratosphere (high-top models) and some evidence was obtained that these models are able to simulate the surface response during northern winter better than low-top models. However, as a whole, most of the high-top models did not reproduce either the magnitude or latitudinal gradients of solar-induced temperature responses in the upper stratosphere that are estimated using most meteorological reanalyses (also Mitchell *et al.*, 2014b). For this reason, the high-latitude dynamical responses that lead to significant top-down forcing of regional surface climate were also not well simulated in most of the high-top models.

In this article, the model characteristics which yield a reasonable agreement of solar signals with available observations of the stratosphere are examined further. Specifically, MLR is applied to compare in more detail solar signals in a subset of the 13 high-top CMIP-5 models considered in Article 1, i.e. the six models that included coupled interactive ozone chemistry (as opposed to those whose stratospheric ozone variability was prescribed *a priori*). Attention is focused especially on the model response of stratospheric ozone (which was not considered in Article 1), as well as those of temperature and zonal wind, and comparisons are made to selected observational estimates for the time period after 1979 when continuous global satellite remote-sensing measurements began.

In many respects, this study builds on a previous work by Austin *et al.* (2008; also Chapter 8 of SPARC-CCMVal, 2010). The latter authors analyzed solar cycle signals of ozone and temperature in a series of simulations of coupled chemistry–climate models (i.e. general circulation models with coupled interactive chemistry) over various periods during the last half of the twentieth century. The employed models did not have coupled oceans but were forced at their lower boundaries using observed sea surface temperatures (SSTs). It was shown that the model ozone results were generally in agreement with observations at tropical latitudes (e.g. Soukharev and Hood, 2006), yielding a double-peaked vertical structure with a maximum response near 3–4 hPa of 2–3% over a solar cycle, a minimum near 20 hPa, and a secondary maximum in the lower stratosphere. The upper stratospheric response is primarily a consequence of increased photolytic ozone production while the lower stratospheric response is believed to have a transport origin, resulting mainly from a slowing of the upwelling branch of the mean meridional (Brewer–Dobson) circulation near solar maxima (Kodera and Kuroda, 2002; Hood and Soukharev, 2012).

However, a long-standing issue is whether part or all of the tropical lower stratospheric 11-year response derived from observations during the satellite era may be a consequence of aliasing from the aerosol effects of two major volcanic eruptions, El Chichòn and Pinatubo, which fortuitously occurred following solar maxima in 1982 and 1991 (Solomon *et al.*, 1996; Lee and Smith, 2003; Chiodo *et al.*, 2014). Austin *et al.* (2008) tested this by comparing solar regression results with and without inclusion of an aerosol term in the MLR statistical model. They found little impact when analyzing model data over the 1960–2005 model period.

But some model chemistry schemes may be more sensitive to volcanic aerosol injections than others. For example, Dhomse *et al.* (2011) analyzed transient simulations using the SLIMCAT chemical transport model developed at the University of Leeds (Chipperfield, 1999, 2006) over 1979–2005 and found that the modelled ozone solar response in the tropical lower stratosphere is amplified by aliasing from the volcanic eruptions. This was apparently because the model overestimates ozone losses during high aerosol loading periods. Therefore further investigation is needed of the volcanic aerosol aliasing issue in coupled climate models.

In section 2, the six high-top CMIP-5 models with interactive ozone chemistry are described and the MLR statistical method which is applied to the model data is summarized. Results of the analysis for annually averaged monthly solar regression coefficients for stratospheric ozone and temperature over the 1979–2005 period are presented and compared for the six models in section 2.5. Annual mean MLR analyses of model data are also carried out for time periods prior to 1979 when there were no major volcanic eruptions to assess further the sensitivity of the different model MLR results to volcanic aerosol aliasing during the 1979–2005 period. In section 3, previous efforts to estimate observationally the 11-year solar-induced responses of stratospheric ozone, temperature, and zonal wind using data acquired after the initiation of continuous global satellite measurements in 1979 are first briefly reviewed. Then, selected observation-based estimates for these responses are presented for comparison with the model results. Next, the

Table 1. High-top CMIP-5 models with interactive chemistry.

Model	Ensemble members	Resolution		Model top (km)	QBO?	Reference
		vertical* (km)	horizontal (°)			
CESM1-WACCM	4	2–3	1.9×2.5	∼140	Nudged	Marsh *et al.* (2013)
MIROC-ESM-CHEM	1	∼1.1	2.8×2.8	∼91	Spontaneous	Watanabe *et al.* (2011)
MRI-ESM1	1	∼2.5	∼1.1	∼86	None	Yukimoto *et al.* (2011)
GFDL-CM3	5	2–3	∼2.0	∼86	None	Donner *et al.* (2011)
GISS-E2-H	5	∼2.0	2.0×2.5	∼66	None	Shindell *et al.* (2013)
GISS-E2-R	5	∼2.0	2.0×2.5	∼66	None	Shindell *et al.* (2013)

*Value in the upper stratosphere near 40 km altitude.

11-year solar signals in ozone, temperature, and zonal wind for the six models are examined in more detail for the northern early winter (November–December) and southern midwinter (July–August) periods when observations indicate the strongest solar-induced latitudinal gradients in ozone/temperature and the largest enhancements of the polar night jet in both hemispheres. A summary and further discussion are given in section 4.

2. Models, statistical method, and annual mean results

2.1. Models

Table 1 lists the six high-top CMIP-5 models with interactive chemistry which are considered here. The institutes mainly responsible for producing these models are:
CESM1-WACCM: National Center for Atmospheric Research, Boulder, Colorado, USA;
MIROC-ESM-CHEM: University of Tokyo, NIES, and JAMSTEC, Japan;
MRI-ESM1: Meteorological Research Institute of Japan, Tsukuba City, Japan;
GFDL-CM3: National Oceanic and Atmospheric Administration, Geophysical Fluid Dynamics Laboratory, Princeton, New Jersey, USA;
GISS-E2-H and GISS-E2-R: National Aeronautics and Space Administration, Goddard Institute for Space Studies, New York, USA.
The two GISS models differ only in the nature of the coupled ocean model (Shindell *et al.*, 2013). The GISS-E2-R model used the 'Russell' ocean (Russell *et al.*, 1995) while the GISS-E2-H model used the Hybrid Coordinate Ocean Model (Sun and Bleck, 2006). All models were required to produce at least one 'historical' simulation over the 1850–2005 period with observed forcing consisting of solar spectral irradiance variations, volcanic sulphate aerosol, and greenhouse gas emissions (Taylor *et al.*, 2012). Effects of energetic charged particle precipitation were generally not included, except for WACCM, which has a parametrization for increased odd nitrogen production in the thermosphere as a function of the geomagnetic Kp index (Marsh *et al.*, 2007). All of the models considered here adopted the NRL SSI model (Wang *et al.*, 2005). Two of the models (CESM1-WACCM and GFDL-CM3) also scaled the total solar irradiance (TSI) by a constant factor of 0.9965 to agree with SORCE Total Irradiance Monitor measurements (Kopp *et al.*, 2005).

In Table 1, column 2 lists the number of ensemble members available for analysis for the period after 1979. Three of the models (GFDL-CM3, GISS-E2-H, and GISS-E2-R) were applied to produce an ensemble of five historical simulations each. The remaining three (CESM1-WACCM, MIROC-ESM-CHEM, and MRI-ESM1) performed one historical simulation each. In addition, CESM1-WACCM carried out three shorter simulations for the 1955–2005 period with initial conditions taken from the single historical run (Marsh *et al.*, 2013). Therefore, a total of four members are available for CESM1-WACCM for the period after 1979 when continuous global satellite observations became available. Columns 3 and 4 list the approximate vertical and horizontal spatial resolutions of each model in the stratosphere (∼3 hPa). The vertical resolutions at this level are comparable (∼2–3 km) for all models except for MIROC-ESM-CHEM, which has a resolution near 1 km. The horizontal resolutions are also comparable (several degrees of latitude or longitude at low latitudes) except for MRI-ESM1, which has a higher resolution near 1°. Column 5 lists the approximate model tops. These range from ∼140 km for CESM1-WACCM to ∼66 km for the two GISS models. Column 6 indicates whether each model simulates a QBO and whether the modelled QBO is internally generated (spontaneous) or whether it is forced (nudged) to agree with observational constraints. Four of the models have no QBO while MIROC-ESM-CHEM has a spontaneous QBO and CESM1-WACCM has a nudged QBO. Finally, column 7 lists a recent reference for each model.

2.2. Model radiation and photolysis rate codes

According to published descriptions, all of the six coupled climate models considered here used up-to-date interactive chemistry schemes. The main characteristics of the chemistry schemes for five of the six models (CESM1-WACCM, MIROC-ESM-CHEM, GFDL-CM3, GISS-E2-R, and GISS-E2-H) have been previously described in detail by Eyring *et al.* (2013; their Appendix A). The chemistry scheme used in the MRI-ESM1 model, which provided data to the CMIP-5 archive at a later time, has been summarized by Yukimoto *et al.* (2011); (also Shibata *et al.*, 2005; Deushi and Shibata, 2011). In addition, the model radiation codes, including methods for simulating heating from volcanic aerosols in the lower stratosphere, are described in detail in the references listed in Table 1.

However, the modelled response of stratospheric ozone and temperature to 11-year SSI forcing depends strongly on the detailed treatment of the solar UV irradiance in the 120–300 nm spectral range. Experiments using a 1D radiative–convective–chemical model presented by Shapiro *et al.* (2013; their Figure 2) are helpful for demonstrating that this is the case. In particular, they showed using the NRL SSI dataset that the increase in ozone mixing ratio in the stratosphere caused by an increase in solar UV radiation is mainly due to enhanced ozone production by O_2 photolysis with a maximum near 40 km altitude. The increase in the 40–60 km layer is related to O_2 absorption in the 121–200 nm interval (Schumann–Runge bands), while below 40 km the main spectral contribution is from the Herzberg continuum (200–242 nm). A negative ozone response is expected in the middle mesosphere, driven by the increase of hydrogen radicals resulting from water vapour photolysis by SSI in the SRB and at the Lyman-α line. Both the positive ozone response centred near 40 km and the negative response peaking in the middle mesosphere (∼68 km) have been confirmed observationally using satellite remote-sensing measurements on the solar rotational (∼27 day) time-scale (e.g. Hood, 1986; Keating *et al.*, 1987; Hood *et al.*, 1991). The absorption at the Lyman-α wavelength by O_2 is also responsible for a strong expected ozone increase in the upper mesosphere. Ozone photolysis in the 240–300 nm spectral

range leads to ozone loss partly compensating the influence of enhanced O_2 photolysis above 30 km.

The expected temperature response to an enhancement of solar UV radiation is always positive and has two maxima at the stratopause and mesopause (e.g. Shapiro *et al.*, 2013). The mesopause maximum is defined mostly by oxygen absorption in the SRB and in the Lyman-α line. In the 50–70 km layer, the SRB and Herzberg continuum contribution dominates, while below 50 km, ozone absorption in the Herzberg continuum and Hartley bands (200–300 nm) is the main contributor to the overall heating.

For regions where the influence of dynamics is not crucial (e.g. the tropical middle to upper stratosphere and lower mesosphere), differences in modelled ozone and temperature responses to increases in SSI can potentially be explained by different representations of the photolysis and radiative heating responses. Therefore, a detailed consideration of the individual model codes is necessary. However it should be noted that the magnitude of the thermal response depends not only on the details of the short-wave radiation codes but also on the quality of the long-wave part of the codes because the net temperature change is a balance between solar heating and infrared cooling.

2.2.1. CESM1-WACCM

The model version participating in CMIP-5 is described by Marsh *et al.* (2013). For wavelengths >200 nm and at altitudes below 65 km, the heating rates are calculated using the scheme of Briegleb (1992), which is based on the two-stream delta-Eddington approximation (also Briegleb and Light, 2007). The solar visible and UV (200–700 nm) spectrum is divided into eight spectral intervals. At UV wavelengths (200–350 nm), only ozone absorption is taken into account to calculate heating rates. At altitudes above 65 km, the WACCM radiation code also directly calculates the heating rates due to ozone and molecular oxygen absorption in the UV (124–400 nm). The employed spectral resolution in this case is much higher and the UV interval is divided into 40 spectral bins. At 65 km, the two sets of heating rates are merged. The photolysis rates are calculated using a look-up table which consists of photolysis rates pre-calculated with the Stratospheric and Tropospheric Ultraviolet and Visible (STUV) radiative transfer model as a function of solar zenith angle, column overhead ozone, surface albedo, temperature, and pressure (SPARC-CCMVal, 2010, their Table 6s-4). The model applies a four-stream discrete ordinate approach for calculations in the spectral interval 120–750 nm, divided into 100 spectral bins. The WACCM also includes photolysis rates in the Schumann–Runge bands (Minschwaner and Siskind, 1993; Koppers and Murtagh, 1996) and Lyman-α line (Chabrillat and Kockarts, 1997). A possible minor weakness of the applied codes is the neglect of molecular oxygen absorption in the UV below 65 km. However, the effect of this on the heating rate response for a nominal solar cycle SSI change is essentially negligible at these altitudes (Figure 3 of Sukhodolov *et al.*, 2014).

2.2.2. MIROC-ESM-CHEM

Radiative heating and photolysis rates are calculated using the radiation code described by Sekiguchi and Nakajima (2008). The radiative transfer solver is based on the two-stream approximation in the form of a discrete-ordinate/adding method and allows treatment of multiple scattering and absorption/emission. The absorption is treated using a correlated k-distribution (CKD) approach. The entire solar spectrum is divided into 23 intervals but the most important ones for the stratosphere/mesosphere solar UV spectrum (185–300 nm) consist of six intervals where the absorption by O_3 and O_2 is included. Photolysis rates are calculated online using temperature and radiation fluxes computed in the radiation code considering absorption and multiple scattering (Watanabe *et al.*, 2011). The cross-sections and quantum yields of the atmospheric species for each spectral bin are calculated using optimized averaging.

Weaknesses of the applied code include absence of the Lyman-α line and water vapour photolysis. This could potentially lead to some overestimation of the ozone response in the upper stratosphere due to absence of H_2O photolysis in the SRB. At altitudes above 60 km, the neglect of the Lyman-α line would result in problems in the simulation of both the ozone and temperature responses.

2.2.3. MRI-ESM1

The model version participating in CMIP-5 is described by Adachi *et al.* (2011). The calculation of heating rates in this version is performed with the two-stream delta-Eddington approximation with the entire solar spectrum divided into 22 spectral intervals (Yukimoto *et al.*, 2011, 2012). The absorption of solar UV radiation by O_2 and O_3 is included following the method of Freidenreich and Ramaswamy (1999), which divides the spectrum from 173 to 400 nm into 11 intervals. Absorption in the molecular lines is treated using a CKD approach. The photolysis rate calculation is based on the scheme applied in the NCAR 2D model SOCRATES* (Huang *et al.*, 1998) and includes all reactions important for the stratosphere and mesosphere. The only obvious weakness of the radiation code is the absence of the Lyman-α line.

2.2.4. GFDL-CM3

The model version participating in CMIP-5 is described by Donner *et al.* (2011). The applied radiation code is based on an original algorithm presented by Freidenreich and Ramaswamy (1999). To improve performance, the code was slightly simplified by reducing the total number of spectral intervals covering the solar spectrum from 25 to 18. However, in the UV range (173–300 nm), the number of intervals remains the same as in the original scheme (Anderson *et al.*, 2004). Clear-sky photolysis rates are calculated using a multivariate interpolation table derived from the TUV model of Madronich and Flocke (1998), with an adjustment applied for the effects of large-scale clouds. As in MRI-ESM1, the only obvious weakness of the radiation code is the absence of the Lyman-α line. However, after the CMIP-5 runs using this model version were complete, a coding error was discovered that resulted in a reference (climatological) solar flux being used by the chemistry code to calculate photolysis rates instead of the actual (time-varying) solar flux (L. Horowitz, 2015; personal communication). Consequently, ozone in GFDL-CM3 does not respond significantly to changes in solar forcing.

2.2.5. GISS-E2-H and GISS-E2-R

The model versions participating in CMIP-5 are described by Schmidt *et al.* (2014). As noted in section 2.1, the GISS H and R versions differ only in the nature of the coupled ocean model. The calculation of heating rates is based on the Lacis and Hansen (1974) parametrization, which considers solar UV absorption only by ozone. The photolysis rates are calculated using the Fast_J2 code of Bian and Prather (2002), which takes into account the model distribution of clouds, aerosols, and ozone. The scheme was improved by adding photolysis of water and NO at high altitudes. The weakness of the applied radiation code is absence of oxygen absorption, which is very important in the upper stratosphere/mesosphere. Possible incomplete representation of the SRB and Lyman-α line in the Fast_J2 code could also lead to an underestimation of the positive ozone and temperature response above 40 km. This underestimation could be enhanced by the

*Simulation of Chemistry, Radiation, and Transport of Environmentally important Species.

added photolysis of water vapour, which provides additional active hydrogen during solar maximum years.

2.3. Long-term mean ozone, temperature, and zonal wind

Prior to discussing the 11-year solar signals in the models, it is first useful to compare long-term mean ozone, temperature, and zonal winds for the individual models to available observation-based estimates. Figure S1(a) shows the annual and zonal mean ozone at latitudes up to 80° derived from observations over 1980–1991 by Fortuin and Kelder (1998). Specifically, zonal mean climatological ozone profiles were estimated using a combination of balloon (ozonesonde) data at levels below 10 hPa and satellite observations from the Solar Backscattered Ultraviolet (SBUV) and Total Ozone Mapping Spectrometer (TOMS) instruments on Nimbus 7. A peak annual mean volume mixing ratio of ∼9.5 ppmv occurs in the equatorial middle stratosphere at 32–35 km altitude. Figure S1(b) shows the annual mean temperature calculated from the ERA-Interim reanalysis dataset over the 1979–2012 period after adjustment to minimize artificial discontinuities as described in the Appendix. Results are shown up to 1 hPa, which is the highest level available for public access. The cold tropical tropopause has a mean temperature of less than 195 K while the stratopause temperature is more than 265 K. Finally, Figure S1(c, d) show the mean zonal wind for the months of December and July calculated from the same reanalysis dataset. Near 1 hPa, the polar night jet peaks at more than 55 m s^{-1} near 45°N in December and reaches more than 95 m s^{-1} near 45°S in July.

Figures S2–S5 contain corresponding model results for comparison to Figure S1. Figure S2 shows the annual mean ozone volume mixing ratio for the six models of Table 1, as calculated from the first archived historical simulation for each model. All of the models produce a reasonable annual mean ozone distribution, although the maximum in the middle stratosphere is noticeably more extended in latitude for the two GISS models. In the upper stratosphere near 1 hPa, the mean ozone mixing ratios according to the MIROC-ESM-CHEM and GFDL models are up to 30% larger than is estimated observationally in Figure S1(a) (∼4 versus ∼3 ppmV). Figure S3 shows the annual mean temperatures for the six models. All distributions are again reasonable up to the stratopause. Above the stratopause, the MIROC-ESM-CHEM mean temperature drops rapidly with altitude, despite the larger ozone concentrations seen in Figure S2(b). The stratopause temperatures for all models are comparable to those estimated from ERA-Interim data in Figure S1(b). Figure S4 shows the December mean zonal wind for the six models while Figure S5 shows the July mean zonal wind. Comparing the December model winds with the corresponding ERA-Interim winds of Figure S1(c), all model wind distributions are reasonable. However, the peak wind near the stratopause for the two GISS models has a somewhat low amplitude (∼35 versus ∼50 m s^{-1}) and is shifted equatorward compared to most of the other models. Similarly, the July mean zonal wind for the two GISS models has a maximum amplitude of about half (∼45 m s^{-1}) of that estimated from observations in Figure S1(d) (∼95 m s^{-1}). Peak July zonal winds for the remaining models are near 90 m s^{-1} except for CESM1-WACCM, which is somewhat high at ∼130 m s^{-1}. Possible reasons for these differences are briefly discussed in section 6.

2.4. Method of analysis

As in Article 1, in order to estimate the 11-year solar component of variability in the model ozone, temperature, and zonal wind monthly mean time series, we adopt a MLR statistical approach. Because the solar signal evolves significantly as a function of season, monthly solar regression coefficients are calculated for comparison to corresponding observational estimates described in section 3. The MLR model applied here differs from that applied in Article 1 only in that the adopted solar predictor (basis function) is the solar Mg II core-to-wing ratio (or Mg II UV index), which is available since 1979 when continuous satellite measurements of SSI began. This index, which consists of a ratio which is insensitive to instrument-related drifts, is a measure of solar UV variations at wavelengths near 200 nm which are important for ozone production in the upper stratosphere (Heath and Schlesinger, 1986; Viereck and Puga, 1999). For example, the correlation coefficient between the Mg II index and the NRL SSI at 205 nm is 0.995. It is demonstrably more effective (see below and Figure S12) in representing solar-induced signals in observational stratospheric ozone data than other proxies such as TSI, F10.7, or sunspot number. In Article 1, for the purpose of analyzing model stratospheric temperature and zonal wind data, the NRL model TSI was adopted as the solar basis function because, unlike Mg II, it is available for the full historical period (1850–2005) and because the UV component of SSI was not represented uniformly in all of the CMIP-5 models.

Specifically, the adopted MLR model for a given atmospheric variable and month $X(i,t)$ is of the form:

$$\begin{aligned} X(i,t) =& \mu(i) + \beta_{\text{solar}}\text{MgII}(i,t) + \beta_{\text{volcanic}}\text{SATO}(i,t) \\ &+ \beta_{\text{QBO1}}\text{QBO1}(i,t) + \beta_{\text{QBO2}}\text{QBO2}(i,t) \\ &+ \beta_{\text{ENSO}}\text{N3.4}(i,t) + \beta_{\text{trend}}\text{GHG}(i,t) + \text{r}(i,t), \end{aligned} \quad (1)$$

where i is the month of the year ($i = 1, 2, \ldots, 12$), t is the time in increments of years, $\mu(i)$ is the long-term mean for the ith month, Mg II(i,t) is the corresponding value of the Mg II UV index, available from the Laboratory for Atmospheric and Space Physics at the University of Colorado (http://lasp.colorado.edu/lisird/mgii; accessed 28 March 2015), SATO(i,t) is a measure of the volcanic aerosol concentration (updated from Sato *et al.*, 1993), QBO1(i,t) and QBO2(i,t) are the first and second Empirical Orthogonal Functions of the model equatorial (5°S to 5°N) zonal mean zonal wind at levels from 5 to 70 hPa in the stratosphere, N3.4(i,t) is the Niño 3.4 index (defined as the model sea surface temperature anomalies in the region from 5°S to 5°N and from 120°W to 170°W), GHG(i,t) is a time series representative of the concentration of well-mixed greenhouse gases, and r(i,t) is the residual noise term. The coefficients β_{solar}, β_{volcanic}, β_{QBO1}, β_{QBO2}, β_{ENSO}, and β_{trend} are determined by linear least squares regression. Note that the QBO1, QBO2, and N3.4 basis function time series must be calculated from the model data for each individual model prior to application of Eq. (1). For models with no QBO, the QBO terms are set to 0. As described in more detail in Article 1, to correct for autocorrelation of the model data residuals after applying Eq. (1), we use the method of Tiao *et al.* (1990) (also Cochrane and Orcutt, 1949; Garny *et al.*, 2007). However, the correction is relatively minor since the year-to-year autocorrelation of the monthly residuals is not large.

2.5. Annual mean model results

Figure 1 shows annual averages of the monthly solar regression coefficients calculated from model ozone data over the 1979–2005 period for all six models listed in Table 1. These averages are produced by first calculating the monthly regression coefficients and standard deviations for each ensemble member for a given model (four for CESM1-WACCM, one for MIROC-ESM-CHEM, one for MRI-ESM1, and five each for GFDL-CM3, GISS-E2-H, and GISS-E2-R). The ensemble means are then calculated for each model and month (Figures S6–S11). Finally, the ensemble means of the coefficients and standard deviations for each of the twelve months are averaged together for each model at each grid point to produce Figure 1. The starting point of 1979 is determined by the beginning of continuous satellite observations (section 3) while the end point of 2005 is determined by the final year of the CMIP-5 simulations. Ozone regression results are shown only at altitudes above 16 km since the vast majority

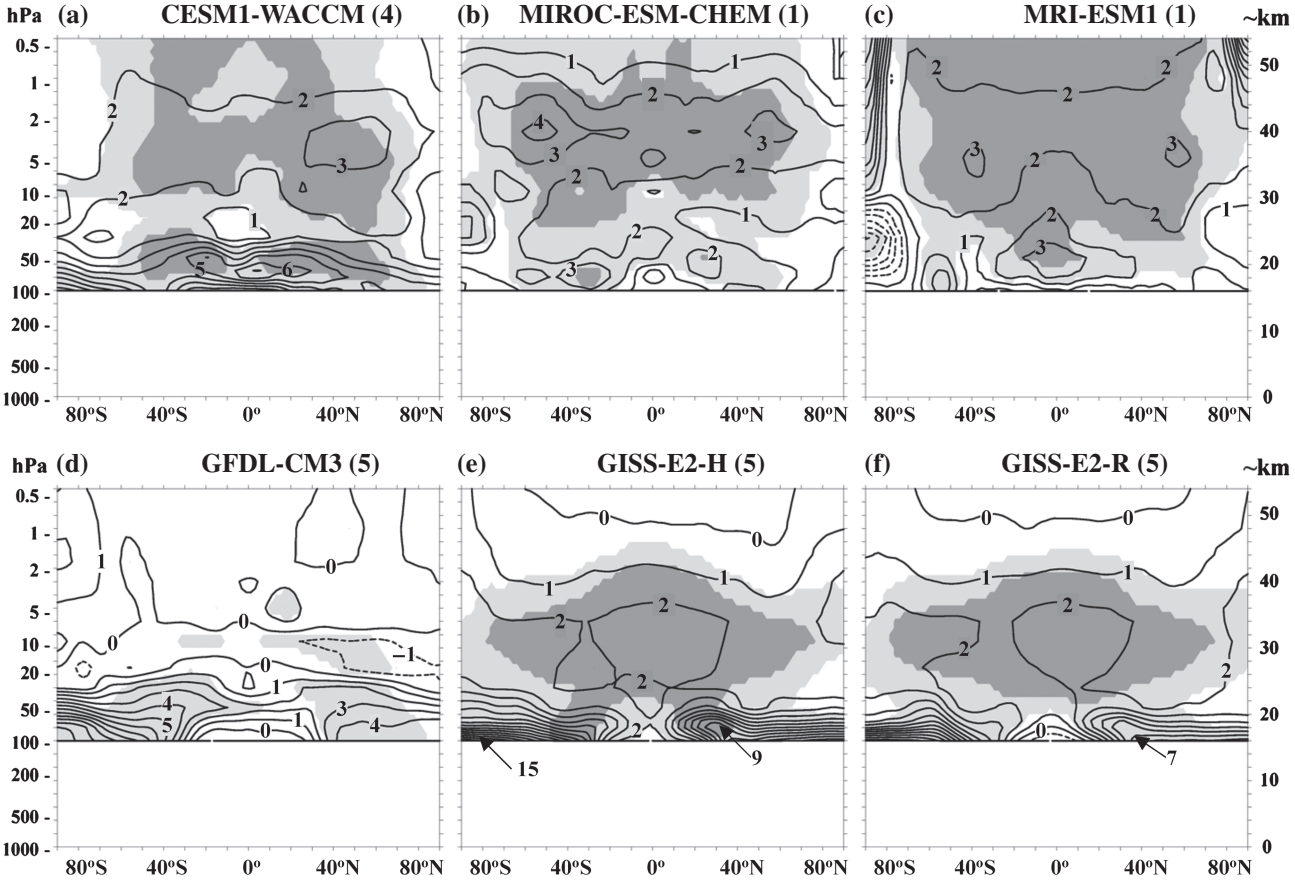

Figure 1. Annual and zonal mean ozone per cent change (max−min) over the 1979–2005 period for the six high-top models with interactive chemistry: (a) CESM1-WACCM, (b) MIROC-ESM-CHEM, (c) MRI-ESM1, (d) GFDL-CM3, (e) GISS-E2-H and (f) GISS-E2-R. Dark (light) shading indicates statistical significance at the 2 (1) sigma level. The contour interval is 1%.

of the ozone column is in the stratosphere. Results are not shown above 54 km since, for four of the six models, output is provided only to approximately this level.

Ozone solar regression coefficients are expressed as the per cent change in ozone concentration or mixing ratio for a change in the Mg II core-to-wing ratio of 0.0169. The latter value is roughly equivalent to a change in F10.7 of ∼130 flux units or a change in sunspot number of ∼130, i.e. it corresponds to a cycle that is about average for the 1940–2000 period but stronger than average for the 1850–1940 period. In the remainder of this article, this change is referred to as solar 'minimum to maximum' or 'max−min'. In this and subsequent figures, dark shaded areas indicate regions where the averaged monthly solar regression coefficients are greater than twice the averaged monthly standard deviations. These areas are statistically significant at approximately 95% confidence. Lighter shaded areas indicate regions where the coefficients are more than one averaged monthly standard deviation and are significant at approximately 68% confidence.

Figures S6–S11 show the monthly ensemble mean ozone solar regression coefficients for each of the six models that were averaged together to produce the annually averaged plots in Figure 1. Figure S12 confirms that the Mg II solar UV index gives more significant ozone solar coefficient regression results for the CMIP-5 model ozone data over the 1979–2005 period. It compares the annually averaged monthly ozone solar regression coefficients obtained for the CESM1-WACCM model when the assumed solar basis function consists of (a) TSI, (b) F10.7, and (c) the solar Mg II UV index. Both the amplitude and statistical significance of the solar regression coefficients are largest when the Mg II UV index is used. Nevertheless, the TSI index used in Article 1 for atmospheric variables other than ozone over the 1850–2005 period remains a valid solar proxy.

As seen in Figure 1, there is a wide range in the amplitude and statistical significance of the ozone solar regression results among the models, especially in the upper stratosphere. Despite the short 27-year analysis period, statistically significant solar coefficients are obtained for five of the six models. Results for models with little or no response in the upper stratosphere are shown in Figure 1(d)–(f). Overall, the least significant coefficients were obtained for GFDL-CM3 while the most significant coefficients were obtained for MRI-ESM1. The GFDL-CM3 results are not significant at the 2σ level with only marginally significant (1σ) values obtained in the lower stratosphere. The two GISS-E2 models produce a significant ozone response with maximum averaged amplitude of ∼2% which is centred in the middle stratosphere near 10 hPa (∼32 km) while the response above 2 hPa is nearly 0.

The three models that do produce a significant averaged upper stratospheric response yield results shown in Figure 1(a)–(c). The CESM1-WACCM response is centred at roughly 4 hPa (∼38 km) while the MIROC-ESM-CHEM and MRI-ESM1 responses are centred at a slightly higher level of 3 hPa or ∼40 km. In all three cases, the peak amplitude averaged over all months is near 3%. Above the stratopause (∼1 hPa), the MRI-ESM1 response is largest (>2%) at high latitudes in both hemispheres.

As also seen in Figure 1, several models (CESM1-WACCM and GISS-E2-H) produce strong and apparently significant ozone responses in the lower stratosphere (∼50 hPa). On the other hand, MIROC-ESM-CHEM and MRI-ESM1 produce reduced and much less significant responses at this level, indicating that the modelled lower stratospheric ozone response could be sensitive to details of the model formulation. In particular, because the time period considered here includes two major volcanic eruptions (El Chichòn in 1982 and Pinatubo in 1991) which followed solar maxima in 1980 and 1989, it is possible that the lower stratospheric ozone signal in many of the models of Figure 1 is affected by aliasing, i.e. lack of complete orthogonality between the solar and volcanic aerosol basis function time series (Solomon *et al.*, 1996; Lee and Smith, 2003). If so, then the magnitude of

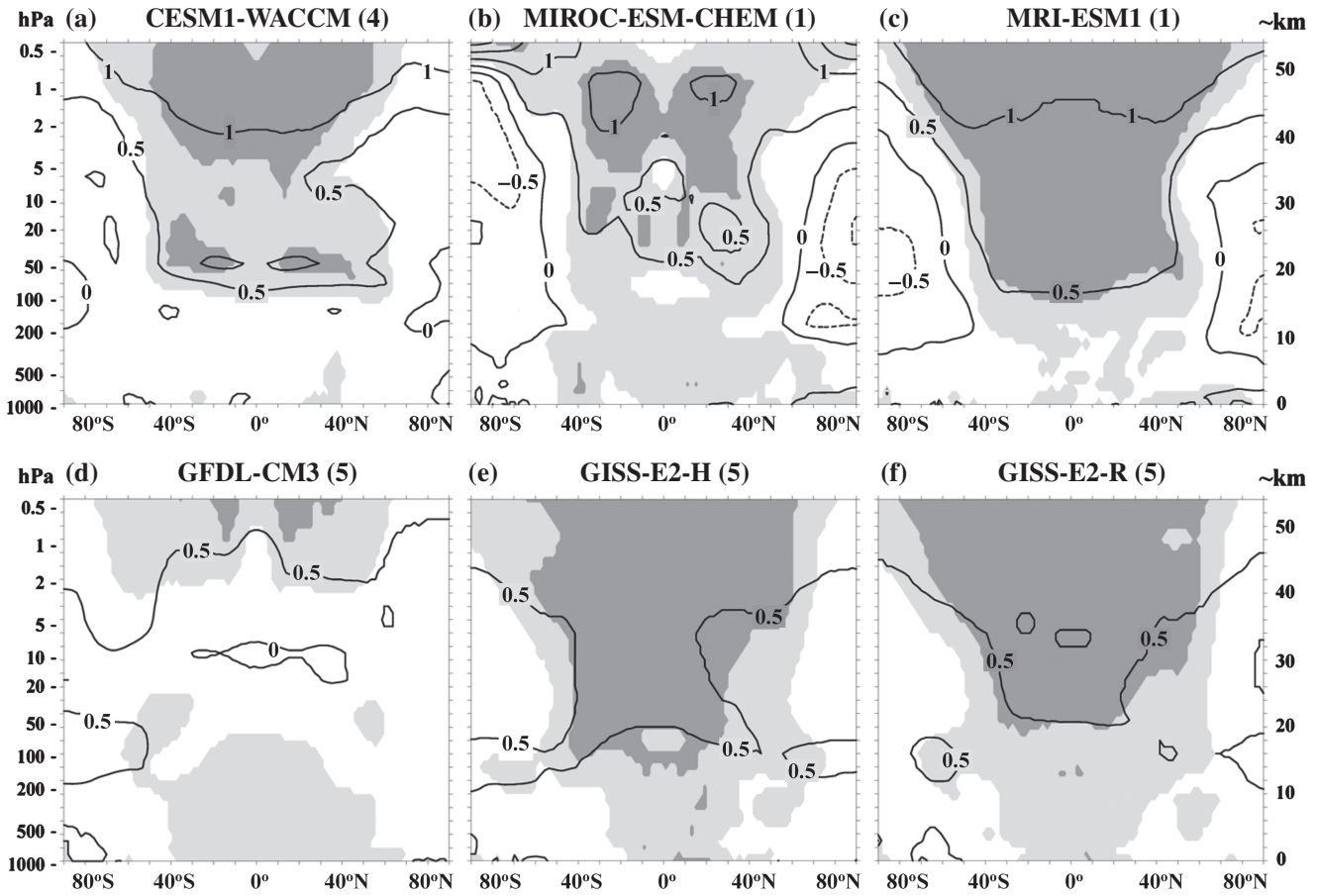

Figure 2. As Figure 1, but for the annual and zonal mean temperature change (max−min) over the 1979–2005 period.

the apparent lower stratospheric 11-year ozone response in many of the models of Figure 1 could be a function of how sensitive the simulated lower stratospheric chemistry and dynamics are to volcanic aerosol effects (e.g. enhanced heterogeneous chemical ozone losses or radiative heating).

The extent to which aliasing between the solar and volcanic aerosol regression coefficients may occur in a version of WACCM (WACCM3.5) without a coupled ocean (forced using observed SSTs and sea ice concentrations) has recently been investigated by Chiodo *et al.* (2014). By carrying out simulations over the 1960–2004 period with and without including volcanic aerosol forcing, it was found that most of the apparent solar-induced variation of tropical lower-stratospheric ozone and temperature in the model is due to the two major volcanic events mentioned above. It was therefore inferred that the part of decadal variability in tropical lower-stratospheric observations which can be attributed to solar variability may be smaller than previously believed. This may indeed be the case (section 3).

However, the results of Figure 1 also suggest that any conclusions drawn from model simulations about the extent of volcanic aerosol aliasing in observations over the 1979–2005 period may depend on the model that is employed. To examine this possibility further, Figure S30 shows results of an MLR analysis of the same model ozone data over the 1955–1981 period (prior to the El Chichòn eruption). The 11-year ozone responses for all models are somewhat weaker at most altitudes than that shown in Figure 1, possibly because of a relatively weak solar cycle 20, which peaked near 1970. But the most dramatic reduction in the response occurs in the lower stratosphere for four of the six models, CESM1-WACCM, GFDL-CM3, and the two GISS models. The remaining two models, MIROC-ESM-CHEM and MRI-ESM1, continue to show a lower-stratospheric response that is proportionally of the same magnitude as obtained for the 1979–2005 period (i.e. the ratio of the lower stratospheric response to the upper stratospheric response is nearly the same). From the combination of Figures 1 and S30, it can be inferred that the former four models produce an 11-year lower stratospheric ozone response which is clearly affected by aliasing from the two volcanic aerosol injection events, while the responses for the latter two are not so strongly affected. However, based only on this comparison of model results, it is difficult to evaluate which set of models is best able to simulate the lower-stratospheric response, the former four or the latter two.

Figure 2 shows corresponding results for the annually averaged monthly temperature solar regression coefficients, expressed as the change (K) from solar minimum to maximum (defined above). The individual ensemble mean monthly temperature solar regression coefficients are plotted in Figures S13–S18 for the six models. The annual mean results of Figure 2 are not very different from those shown in Article 1, which used TSI rather than Mg II as the solar predictor and which analyzed the full suite of CMIP-5 models. Nevertheless, we show them here for completeness. As seen in the figure, the annual mean temperature results resemble the ozone results of Figure 1 since the ozone change contributes significantly to the radiative heating change from solar minimum to maximum in the stratosphere (e.g. Gray *et al.*, 2009).

In the upper stratosphere, the three models in Figure 2(a)–(c) produce the strongest responses, exceeding 1 K near the stratopause. The GFDL-CM3 model produces the least significant results with amplitudes of ∼0.5 K near the stratopause at most latitudes while the MRI-ESM1 model produces the strongest and most significant temperature response throughout the low-latitude stratosphere, exceeding 1 K above the 2 hPa level. The two GISS-E2 models produce a significant temperature response of intermediate amplitude (>0.5 K) at most levels above ∼30 hPa.

In the lower stratosphere at levels between 20 and 50 hPa, all models except GFDL-CM3 produce an apparently significant response of order 0.5 K or more from solar minimum to maximum. However, as discussed above for ozone, it is likely that 11-year signals in the lower stratosphere for many of these models are affected by aliasing from volcanic aerosol injections

during the 1979–2005 period. To test this possibility, Figure S31 shows results of a similar analysis for the 1955–1981 period. The apparently significant subtropical CESM1-WACCM responses at the 50 hPa level seen in Figure 2 are not present in Figure S31 and are replaced by a weakly significant equatorial response centred at about 20 hPa. The lower-stratospheric responses for the MRI-ESM1 model and the two GISS-E2 models seen in Figure 2 are no longer present in Figure S31. Only in the case of the MIROC-ESM-CHEM model does a weak lower-stratospheric response remain in the 20–50 hPa tropical region. Thus, only MIROC-ESM-CHEM and possibly CESM1-WACCM could be simulating a true solar-induced tropical lower-stratospheric temperature response.

Turning to the monthly model ozone and temperature solar coefficients plotted in Figures S6–S11 and S13–S18, a seasonal evolution of the solar-induced signal is clearly present. In the summer hemisphere for all models, the thermal response in the upper stratosphere tends to shift toward higher latitudes, reflecting the reduced solar-zenith angle during that season and the longer duration of daily solar heating at polar latitudes (midnight sun). However, for the models in Figures 1(a)–(c) and 2(a)–(c) with a relatively large upper-stratospheric ozone and temperature response (CESM1-WACCM, MIROC-ESM-CHEM, and MRI-ESM1), there is also a tendency for large negative latitudinal ozone and temperature gradients to develop at high latitudes in the winter hemisphere. A similar tendency for temperature averaged over all high-top models during northern winter was also shown in Figure 7 of Article 1. Averaged over all four of the CESM1-WACCM ensemble members, the large negative ozone and temperature gradients are mainly seen in the Southern Hemisphere (SH) in June and July but are also present in the Northern Hemisphere (NH) winter for two of the four members (not shown). In the case of the single MIROC-ESM-CHEM simulation, it occurs in December at high northern latitudes and in July/August at high southern latitudes for both ozone and temperature. The same is true for the single MRI-ESM1 simulation. For the latter two models, the negative latitudinal gradients are noticeably larger in the SH winter.

3. Comparisons with observational estimates

3.1. Ozone

Continuous global satellite remote-sensing measurements of stratospheric ozone have been obtained since late 1978 (WMO, 2007). These measurements, like those of SSI, are subject to uncertainties including degradation with time and intercalibration offsets between different instruments. The longest continuous record of stratospheric ozone concentrations by a single instrument was obtained by the Stratospheric Aerosol and Gas Experiment (SAGE) II, beginning in November 1984 and ending in August 2005. The solar occultation measurement technique employed by SAGE yields a relatively good vertical resolution approaching 1 km (e.g. McCormick *et al.*, 1989). Analyses of these data indicate substantial variations of 2–4% from solar minimum to maximum extending from ∼5 hPa to and above the stratopause at low latitudes (e.g. Soukharev and Hood, 2006; Randel and Wu, 2007; Kyrölä *et al.*, 2013; Remsberg, 2014; Figure 3(c)). However, due to the sparse sampling of the SAGE solar occultation measurements, only annual mean regression coefficients can be accurately estimated.

A second long-term dataset with more complete sampling but less continuity and less vertical resolution (∼8 km) has been constructed at the US Goddard Space Flight Center by merging together vertical ozone soundings by a series of SBUV instruments on Nimbus 7 (late 1978–1990) and subsequent US National Oceanic and Atmospheric Administration (NOAA) operational satellites (Kramarova *et al.*, 2013; McPeters *et al.*, 2013). The data obtained by the Nimbus 7 SBUV instrument were at a nearly constant local time while data acquired with SBUV/2 instruments

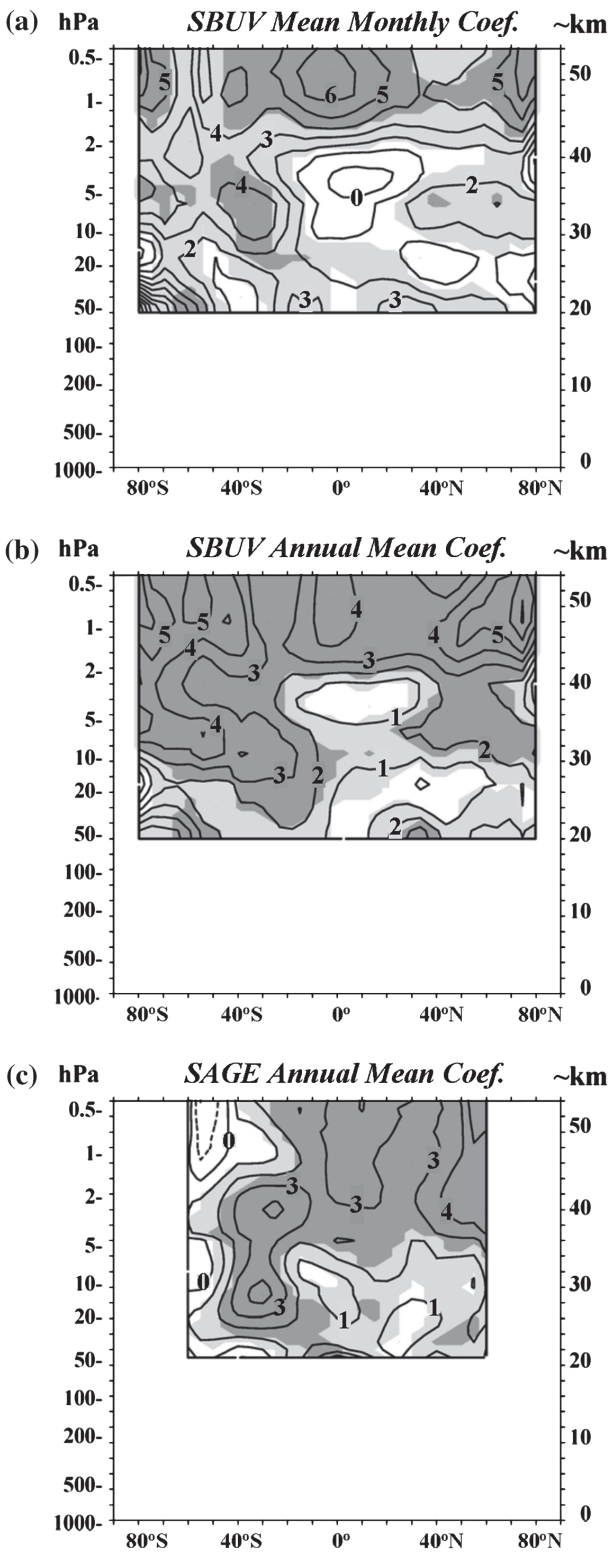

Figure 3. (a) Annually averaged monthly ozone change (max–min) for the version 8 merged SBUV ozone data over the 1979–2003 period. Panel (b) is as (a) but for the annual mean ozone change. Panel (c) shows the annual mean ozone change for the version 6 SAGE II dataset over the 1985–2005 period.

on the NOAA satellites beginning with NOAA 11 in 1989 were more affected by orbital drifts which caused the local time of measurement to vary during many of these missions. In the upper stratosphere (∼2 hPa and above), this can introduce artificial trends since there is a significant diurnal variation of ozone at these levels. MLR analyses of the merged SBUV data through 2003 yield a substantial annual mean solar cycle variation of 3–4% at ∼2 hPa and above in the upper stratosphere at low latitudes (Soukharev and Hood, 2006; Tourpali *et al.*, 2007). As shown in the latter references, seasonal (e.g. northern winter and summer) mean regression coefficients can also be estimated using the more

densely sampled, merged SBUV dataset. However, as discussed further below, the SBUV results have significant uncertainties imposed by the shortness of the data record (no more than 3.5 solar cycles) and the low vertical resolution of the individual profile measurements.

A third dataset of interest is that obtained by the Halogen Occultation Experiment (HALOE) on the Upper Atmosphere Research Satellite (UARS). Like SAGE, this experiment used the solar occultation technique but operated only from late 1991 to late 2005. HALOE retrieved ozone profiles on a pressure coordinate while SAGE ozone was retrieved on height levels, which requires adoption of a long-term temperature record in order to convert the measurements to mixing ratios on pressure surfaces. Analyses of the HALOE ozone profile dataset yield somewhat reduced solar regression coefficients in the upper stratosphere compared to those estimated from the longer SAGE and merged SBUV records (Soukharev and Hood, 2006; Remsberg, 2008). As discussed in the latter references, these reduced coefficients appear to agree better with model estimates near and above the stratopause than those derived from SAGE or SBUV. However, it is unclear whether the reduced coefficients are a consequence of the more direct HALOE retrieval technique or of the shorter record length (14 years).

To allow a more direct comparison with the annually averaged monthly model ozone solar regression coefficients of Figure 1 and the monthly coefficients of Figures S6–S11, the analysis of Soukharev and Hood (2006) was extended to calculate monthly merged SBUV ozone regression coefficients using the same MLR model (1) that was applied to the CMIP-5 model data. Specifically, the monthly mean version 8 merged SBUV ozone profile dataset covering 1979–2003 was reanalyzed to calculate individual monthly solar regression coefficients using the updated statistical model (1), including the more conservative autocorrelation correction described in section 2 and Article 1. The ENSO basis function in this case is the observed Niño 3.4 index and the two QBO empirical orthogonal functions are calculated from the ERA-Interim reanalysis data as described in Article 1. The N3.4 time series is lagged by 3 months to account for the observed delay in the stratospheric response to surface ENSO variability (e.g. Hood *et al.*, 2010). The analysis is limited to the period prior to 2004 to allow direct comparisons with the results of Soukharev and Hood (2006) and Tourpali *et al.* (2007) and to avoid any effects of a drift in the NOAA 16 orbit, which began in early 2004.

Figure 3(a) shows the annually averaged SBUV monthly solar regression coefficients to allow a direct comparison to the model annually averaged coefficients of Figure 1. Specifically, Figure 3(a) was produced by averaging together the twelve monthly SBUV ozone solar regression coefficients and the corresponding standard deviations at each grid point. The individual monthly SBUV solar regression coefficients are plotted in Figure S19. Regression coefficients and standard deviations at a given grid point were calculated from the 25 monthly means over 1979–2003. Figure 3(b) shows the annual mean SBUV solar regression coefficients obtained by considering each monthly anomaly (monthly mean minus long-term monthly mean) as an independent data point ($25 \times 12 = 300$). The annual mean coefficients of Figure 3(b) are more statistically significant than the annually averaged monthly coefficients of Figure 3(a), as would be expected from the increased number of data points. In both cases, the per cent change in ozone from solar minimum to maximum is largest in the uppermost stratosphere, especially in the Tropics and at high latitudes in both hemispheres. In the tropical middle stratosphere (~4 hPa), the response is a minimum and is statistically insignificant. Positive responses are also obtained in the extratropical middle stratosphere and in the lower stratosphere near 50 hPa. The annually averaged monthly and annual mean ozone solar regression coefficients in Figure 3(a, b) are only marginally significant in the lower stratosphere. This differs from the results of Soukharev and Hood (2006) and Tourpali *et al.* (2007), who found apparently significant annual mean coefficients in much of the lower stratosphere. The reduced significance obtained here is probably due to the use of alternate basis functions for volcanic aerosol and the QBO, as well as to the more conservative autocorrelation correction. However, the monthly regression coefficients remain statistically significant during certain months, especially July and August, as seen in Figure S19. Also, analyses of column ozone, which is dominated by lower stratospheric ozone, as a function of longitude and latitude yield significant solar regression coefficients at low latitudes during the northern summer and winter seasons (Hood and Soukharev, 2012).

Comparing the annually averaged monthly SBUV ozone solar regression coefficients of Figure 3(a) with the corresponding model coefficients of Figure 1, none of the models appears to yield an ozone response which agrees to first order with that derived from the SBUV observations. None of the models produces a relative minimum in the tropical response near 4 hPa, although CESM1-WACCM produces a tropical minimum near the 20 hPa level. The averaged monthly SBUV coefficients yield maxima near the stratopause exceeding 6% in the Tropics, decreasing to ~4% at middle latitudes, and increasing again to more than 6% at high latitudes. None of the models produces a response that maximizes near the tropical stratopause with reductions at midlatitudes. The three models in Figure 1(a)–(c) do produce relatively large (>2%) ozone responses in the upper stratosphere but they are centred near 4, 3, and 3 hPa, respectively, while the SBUV response is centred above 1 hPa. The three models in Figure 1(d)–(f) produce responses at even lower levels (centred at or below the 10 hPa level).

However, some of the disagreements between Figures 1 and 3(a) may be a consequence of measurement uncertainties. Although the merged SBUV dataset is the only available record with sufficient sampling and length to allow reasonable estimation of seasonally resolved ozone solar regression coefficients, there could be an artificial bias in these data toward higher altitudes. Evidence that this may be the case comes from a consideration of the annual mean solar regression coefficients obtained from SAGE data, which have much better vertical resolution (~1 km versus ~8 km for SBUV). Figure 3(c) shows the result of an analysis of version 6 SAGE II data (updated from Soukharev and Hood, 2006) using the improved MLR model (1) and autocorrelation correction. In agreement with previous analyses (e.g. Randel and Wu, 2007), the region of minimum tropical response based on SAGE data is centred near 10 hPa (~31 km) while that of Figure 3(b) based on SBUV data is centred near 4 hPa (~38 km). The SAGE-derived ozone solar regression coefficients exceed 2% and are statistically significant at all levels above 5 hPa (~36 km) continuing up to at least 0.5 hPa (~54 km). On the other hand, the annual mean SBUV coefficients of Figure 3(b) exceed 2% in the Tropics only at levels above 2 hPa (~42 km).

Independent evidence that the ozone 11-year solar regression coefficients derived from merged SBUV data are underestimated at levels below 2 hPa in the Tropics has also been presented by Fioletov (2009). He predicted 11-year ozone variations at low latitudes using the observed ozone response to short-term solar rotational (~27-day) UV variations and then compared these projected variations to observed decadal variations in data from the individual SBUV instruments. It was found (Figure 12 of Fioletov, 2009) that the projected variation remained significant down to altitudes as low as 33 km even though no response was detectable in the combined SBUV time series. Also, the SBUV data from the Nimbus 7 time period (1979–1990) contained an anomalously large 11-year variation at altitudes above 44 km compared to the projected variation and to that recorded during later solar cycles.

Accepting the possibility that the actual observed ozone response extends downward to at least the 5 hPa level in the Tropics, the three modelled ozone responses in Figure 1(a)–(c)

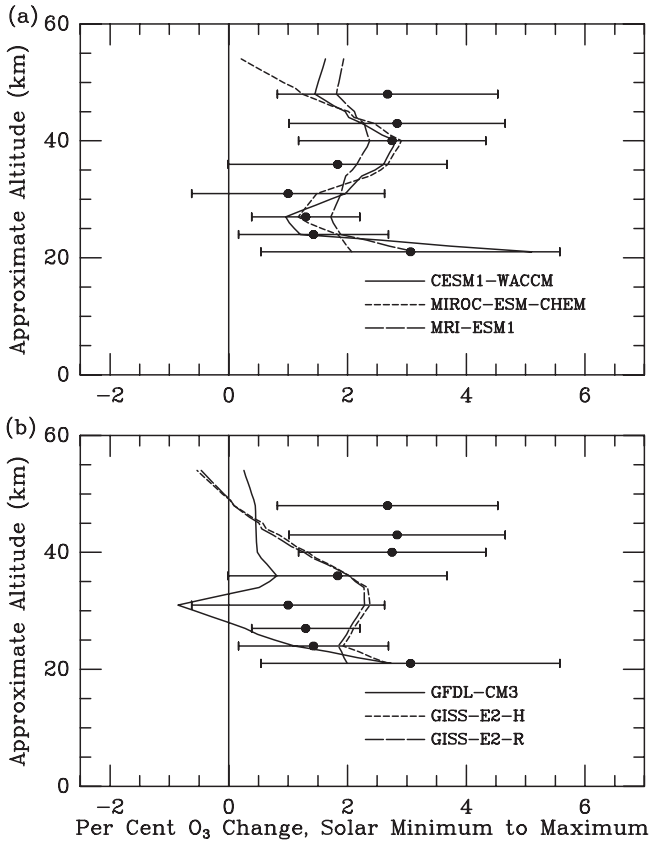

Figure 4. Comparison of tropical (25°S to 25°N) averages of SAGE II annual mean ozone solar regression coefficients (solid circles with 2σ error bars) with similar averages of the annually averaged model solar regression results of Figure 1. Panel (a) is for the three models with a substantial upper-stratospheric ozone response and (b) is for the remaining three models.

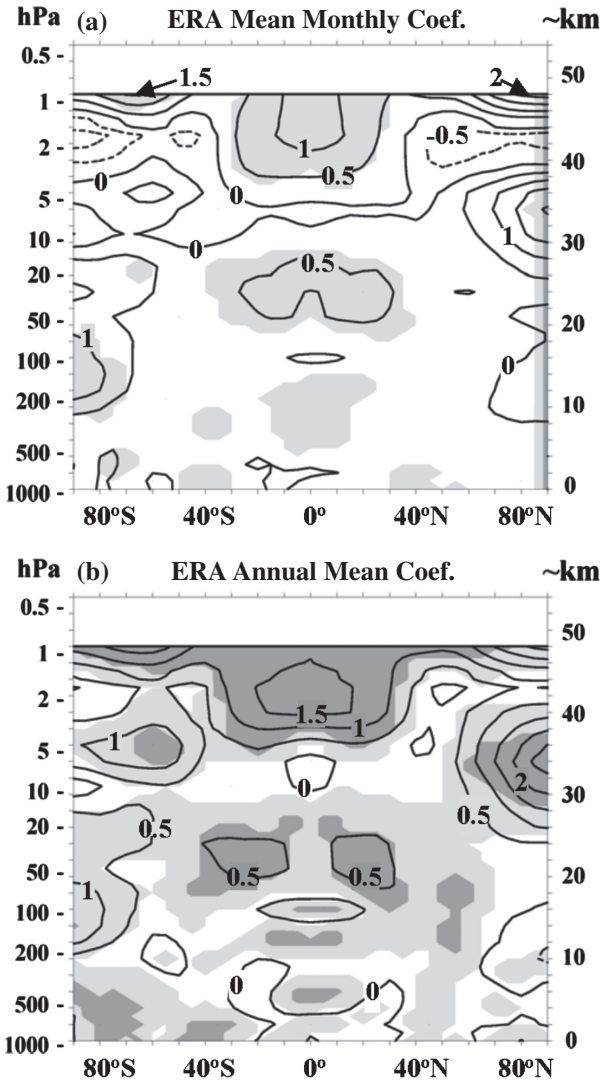

Figure 5. (a) Annually averaged monthly temperature change (max−min) over the 1979–2012 period for the ERA-Interim reanalysis dataset after adjustments for offset step changes in the upper stratosphere. Panel (b) is as (a) but for the annual mean temperature change with each monthly temperature anomaly considered as an independent data point.

compare more favourably with the observations. To illustrate this, Figure 4 plots tropical (25°S to 25°N) area-weighted averages of the SAGE II results from Figure 3(c) at a series of pressure levels up to 1 hPa (∼48 km) together with corresponding averages of the model results of Figure 1. As seen in Figure 4(a), the three models in Figure 1(a)–(c) yield ozone response profiles that fall well within the 2σ error bars of the tropical mean SAGE II solar coefficients. As seen in Figure 4(b), the remaining models produce tropical mean upper-stratospheric ozone responses that are outside of the 2σ error bars at altitudes above 40 km. Also, the altitude dependence of the solar ozone response for the latter models differs noticeably from that estimated from the SAGE II data.

3.2. *Temperature*

Continuous global satellite remote-sensing measurements of atmospheric temperature also began in the late 1970s. In Article 1, model temperature solar responses were compared to estimates derived from the three most recent meteorological datasets, MERRA†, ERA-Interim, and JRA-55‡ (Mitchell *et al.*, 2014b). As discussed in Article 1, a maximum solar-induced temperature response in the reanalyses of several Kelvin is obtained at low latitudes well above the stratopause (∼0.5 hPa), whereas the maximum expected theoretical response is about half this amplitude and is centred near the stratopause (Gray *et al.*, 2009). It was therefore suggested that increased errors in the reanalyses at levels above 1 hPa (where data assimilation is poorly constrained by observations) may be responsible for the unexpectedly large apparent solar signal. A comparison of direct satellite Stratospheric Sounding Unit (SSU) measurements with reanalysis temperature time series supported this inference (Mitchell *et al.*, 2014b).

Here, we consider specifically temperature and zonal wind data from one of the reanalyses, ERA-Interim (Dee *et al.*, 2011), which are publicly available to a level of 1 hPa (http://apps.ecmwf.int/datasets; accessed 29 March 2015). As described in the Appendix (also McLandress *et al.*, 2014), at least one source of error in this dataset (step changes in upper-stratospheric temperature occurring near the times of major changes in instrumentation or processing of assimilated data) can be empirically minimized to produce an 'adjusted' ERA-Interim zonal mean temperature dataset. Such an empirical minimization procedure is not generally applicable to other reanalyses (e.g. MERRA) because step changes were usually replaced with ramp functions in the archived datasets.

Figure 5(a) shows the annually averaged monthly solar temperature regression coefficient derived from the adjusted ERA data over the 1979–2012 period, expressed as the change in Kelvin from solar minimum to maximum as defined in section 2.5. The entire available 34-year record is considered rather than just the 1979–2005 period because the results change only slightly as compared to the shorter record and the statistical significance is improved. The individual monthly ERA-Interim solar temperature regression coefficients are plotted in Figure S20. Figure 5(b) shows the corresponding annual mean coefficient obtained when all available data points ($12 \times 34 = 408$) are

†Modern Era Retrospective Analysis for Research and Applications.
‡Japanese 55-year Reanalysis, 1958–2012.

analyzed. The annual mean tropical upper-stratospheric response is larger in peak amplitude ($\geq$ 1.5 K) and is formally significant while the annually averaged monthly response of Figure 5(a) has a peak amplitude of $\geq$1 K and is only marginally significant. Overall, Figure 5(b) agrees well with previous studies, which analyzed the ERA-40 reanalysis dataset through 2001 or extensions thereof (e.g. Crooks and Gray, 2005; Frame and Gray, 2010). It also agrees well with an alternate analysis of ERA-Interim data by Mitchell *et al.* (2014b). As shown in their Figure 7, the peak response in the Tropics occurs near 2 hPa and the high-latitude maxima at 1 hPa in Figure 5(b) extend up to 0.3 hPa ($\sim$55 km).

Comparing the annual ERA temperature results of Figure 5 with the annual observational ozone results of Figure 3, several similarities are notable. First, in the Tropics, the ozone response is largest in the upper stratosphere (down to $\sim$2 hPa for SBUV and down to $\sim$5 hPa for SAGE) while the temperature response is also largest in the tropical upper stratosphere (1–3 hPa). Second, at high latitudes near the 1 hPa level, the temperature response maxima of order 2 K compare favourably with the SBUV ozone response maxima of order 5–6%. A comparison of the monthly ERA temperature results of Figure S20 with the corresponding SBUV ozone results of Figure S19 shows that the high-latitude responses of both ozone and temperature occur in the summer hemisphere. They are therefore presumably a consequence of the enhanced photolytic and radiative effects of more continuous solar radiation at reduced solar-zenith angles in the polar regions during the summer season. Third, the lower stratospheric subtropical temperature response maxima agree qualitatively with responses seen in the SBUV data at comparable pressure levels, especially when the individual monthly responses are examined. Specifically, as seen in Figure 3(a) for the annually averaged SBUV monthly coefficients, marginally significant ozone response maxima of order 3% are present in the subtropical lower stratosphere near 50 hPa. These coefficients are formally significant with larger amplitudes (up to 8%) during July and August (Figure S19). Similarly, the ERA-Interim monthly coefficients are formally significant with amplitudes >0.5 K near 50 hPa only during June, July, and August (Figure S20).

Comparing the annual temperature responses of Figure 5 with the corresponding model responses of Figure 2, it is first apparent that the three models in Figure 2(a)–(c) yield statistically significant minimum-to-maximum temperature changes in the tropical upper stratosphere which are closer in magnitude (>1 K) to those obtained from the adjusted ERA data. This is further shown in Figure 6, which compares tropical averages of the ERA-Interim temperature solar regression coefficients to similar averages of the model solar coefficients, analogous to the tropical ozone comparison in Figure 4. None of the models, however, produces secondary temperature response maxima at high polar latitudes which are similar to those obtained in the ERA-Interim data. The observationally estimated maxima are likely to be real because they are seen in both hemispheres in summer and correspond to similar polar ozone maxima found in SBUV data. An examination of Figures S13–S18 shows that most of the models (except GFDL-CM3) produce broad maxima in the temperature response at high summer latitudes near the stratopause but the amplitudes are in the range of 1.0–1.5 K, which is less than obtained from the reanalysis data.

As discussed in section 2.5 in relation to Figures 2 and 6, many of the models produce broad positive responses in the tropical lower stratosphere that appear to be statistically significant but are probably influenced by aliasing from the effects of the El Chichòn and Pinatubo volcanic aerosol injection events (and possibly ENSO events). In particular, CESM1-WACCM produces localized subtropical response maxima that are qualitatively similar to those obtained from the ERA-Interim data. It is therefore entirely possible that some of the lower stratospheric thermal response in the ERA-Interim results is also influenced by volcanic aerosol and ENSO aliasing effects. However, the peak amplitudes in the lower stratosphere for CESM1-WACCM ($\sim$1 K) are nearly

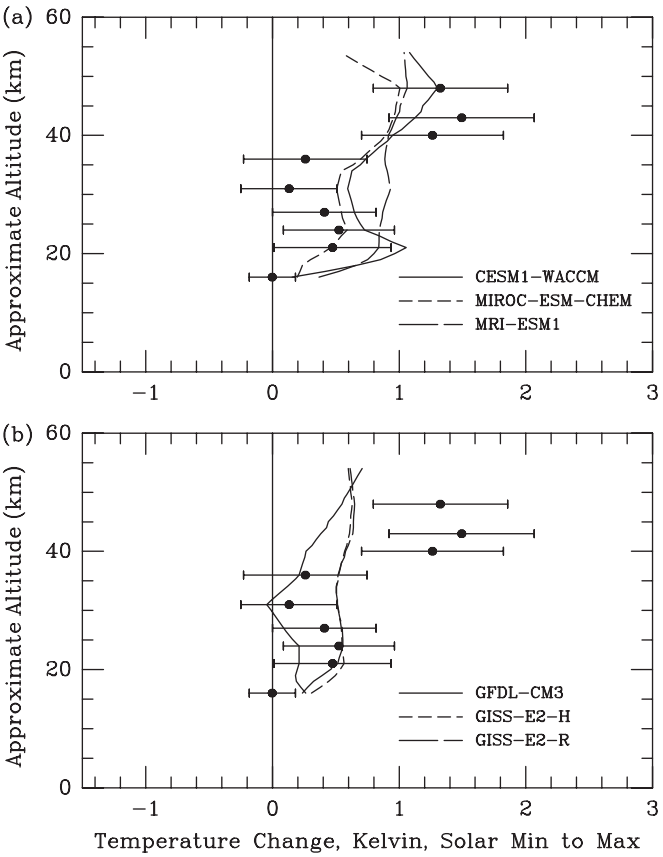

Figure 6. Comparison of tropical (25°S to 25°N) averages of adjusted ERA-Interim annual mean temperature solar regression coefficients (solid circles with 2σ error bars) with similar averages of the annually averaged model solar regression results of Figure 2. Panel (a) is for the three models with a substantial upper-stratospheric ozone response and (b) is for the remaining three models.

a factor of 2 larger than those in Figure 5(b) ($\sim$0.6 K). Also, as seen in Figure S13, the monthly model temperature responses in this location are significant during most months while, as seen in Figure S20, the corresponding observational monthly temperature responses near 50 hPa are significant only during NH summer. Similarly, as seen in Figure S6, the CESM1-WACCM 11-year ozone response in the lower stratosphere is large and significant during nearly all months while, as seen in Figure S19, the observationally estimated tropical ozone response near 50 hPa is significant only during NH summer. Hence, the aliasing effects in the observations could be less than is the case for CESM1-WACCM. Consistent with this possibility, at least one model, MIROC-ESM-CHEM, produces lower stratospheric 11-year ozone and temperature responses with amplitudes during the non-volcanic 1955–1981 period which are comparable to those during the volcanically affected 1979–2005 period (Figures S30(b) and S31(b)). However, as already stated in section 2.5 above, without further information (e.g. investigation of the accuracies of different model sensitivities of lower-stratospheric ozone and temperature to aerosol forcing), it is difficult to evaluate which model, CESM1-WACCM or MIROC-ESM-CHEM, is better able to simulate aliasing effects on observational solar regression coefficients in the lower stratosphere.

3.3. *Zonal wind*

The apparent offset errors found in ERA-Interim temperature data in the upper stratosphere should be less problematic for the derived zonal wind field since the latter depends primarily on latitudinal temperature gradients, which are less sensitive to sudden steps in mean temperatures. The MLR model (1) was therefore applied to the ERA-Interim zonal wind data over 1979–2012 to obtain the monthly solar regression coefficients plotted in Figure S21. Again, we consider the extended time

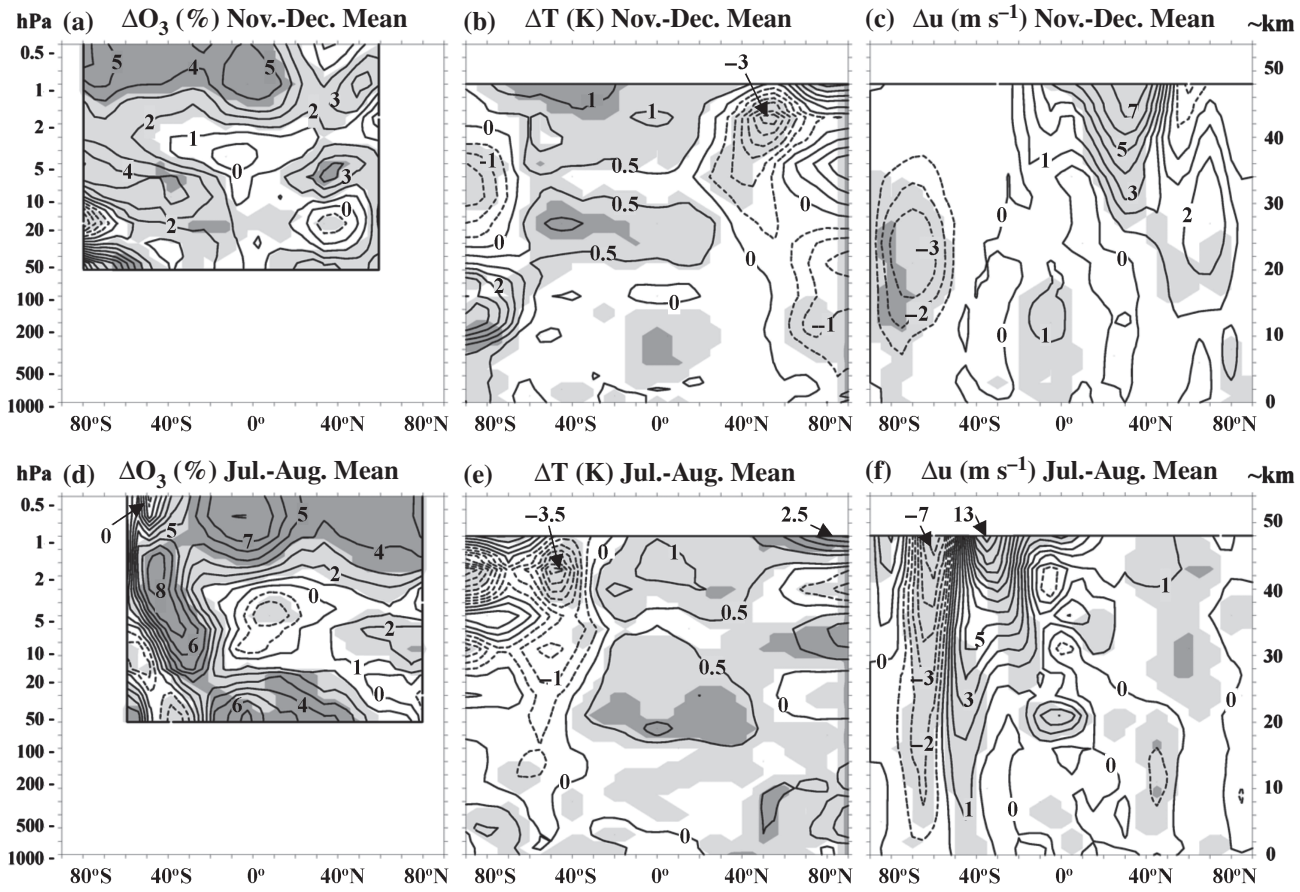

Figure 7. Observationally estimated solar cycle change (max−min) in zonal mean ozone, temperature, and zonal wind during (a)–(c) early northern winter and (d)–(f) middle southern winter (see text). The contour interval is 1% for ozone, 0.5 K for temperature, and 1 m s^{-1} for zonal wind.

period because the results are very similar to those obtained for 1979–2005 and the statistical significance is slightly increased. The regression coefficients are expressed as the change in the zonal wind in m s^{-1} from solar minimum to maximum, as defined in section 2.5.

As seen in Figure S21, the ERA-Interim zonal wind solar regression coefficients are only marginally significant during most months but are characterized by a consistent dependence on season in both hemispheres. Specifically, the largest zonal wind changes from solar minimum to maximum are estimated to occur at northern and southern midlatitudes in the uppermost stratosphere during the winter season of each hemisphere. During northern winter, the largest positive zonal wind response (up to 9 m s^{-1}) is obtained during November and December while, during southern winter, the largest positive response (up to 15 m s^{-1}) is obtained during July and August. During some of these months (December, July, and August), the positive zonal wind response at subtropical to middle latitudes is complemented by a weaker negative response at higher latitudes. In February, a large negative response (up to −17 m s^{-1}) is obtained near the stratopause at ∼70°N. As suggested for example by Gray *et al.* (2004) (also Mitchell *et al.*, 2014b), the latter negative response in late winter may reflect an increased tendency for major stratospheric warmings to occur later in the winter under solar maximum conditions when the polar vortex in early winter is stronger, on average, and less disturbed. These results are similar to those obtained previously by Frame and Gray (2010) using ERA-40 reanalysis data and operational analyses for the 1979–2008 period (their Figure 7) and by Mitchell *et al.* (2014b) using nine different reanalysis datasets. The existence of 11-year wintertime positive zonal wind anomalies in the midlatitude upper stratosphere was first reported based on rocketsonde data by Kodera and Yamazaki (1990). Later investigations of stratospheric data compiled by the former US National Meteorological Center found evidence for a similar dynamical response in the southern winter (Hood *et al.*, 1993). The existence of a positive upper-stratospheric zonal wind response to solar forcing during early winter is a basic element of the top-down mechanism for solar-induced regional climate change (Kodera and Kuroda, 2002; Matthes *et al.*, 2006).

Because the observationally estimated positive zonal wind response is a maximum during NH early winter (November and December) and SH middle winter (July and August), Figure 7 shows the mean ozone, temperature, and zonal wind responses for these particular time periods. This figure is intended to illustrate the basic seasonal dependence of the observed solar signal in the stratosphere during early to middle winter. The positive zonal wind responses in both hemispheres at these times are accompanied by strong negative latitudinal gradients in the ozone and temperature responses which are centred approximately on the latitude of the zonal wind response.

3.4. *Seasonal model comparisons*

Finally, we wish to compare in more detail the seasonal ozone, temperature, and zonal wind responses obtained from the six high-top CMIP-5 models with interactive chemistry to the observationally estimated responses of Figure 7. The main objective is to determine whether the three models in Figures 1(a)–(c), 2(a)–(c), 4(a), and 6(a) which produce substantial upper stratospheric ozone and temperature responses also produce a seasonally dependent response of ozone, temperature, and zonal wind which compares favourably with observations. For this purpose, the monthly solar regression results for zonal wind for each of the six interactive models of Table 1 are plotted in Figures S22–S27.

Prior to considering the six interactive models of Table 1, it is useful to consider an ensemble of three simulations performed by a high-top model without interactive chemistry (MIROC-ESM). This model is a version of MIROC-ESM-CHEM but without

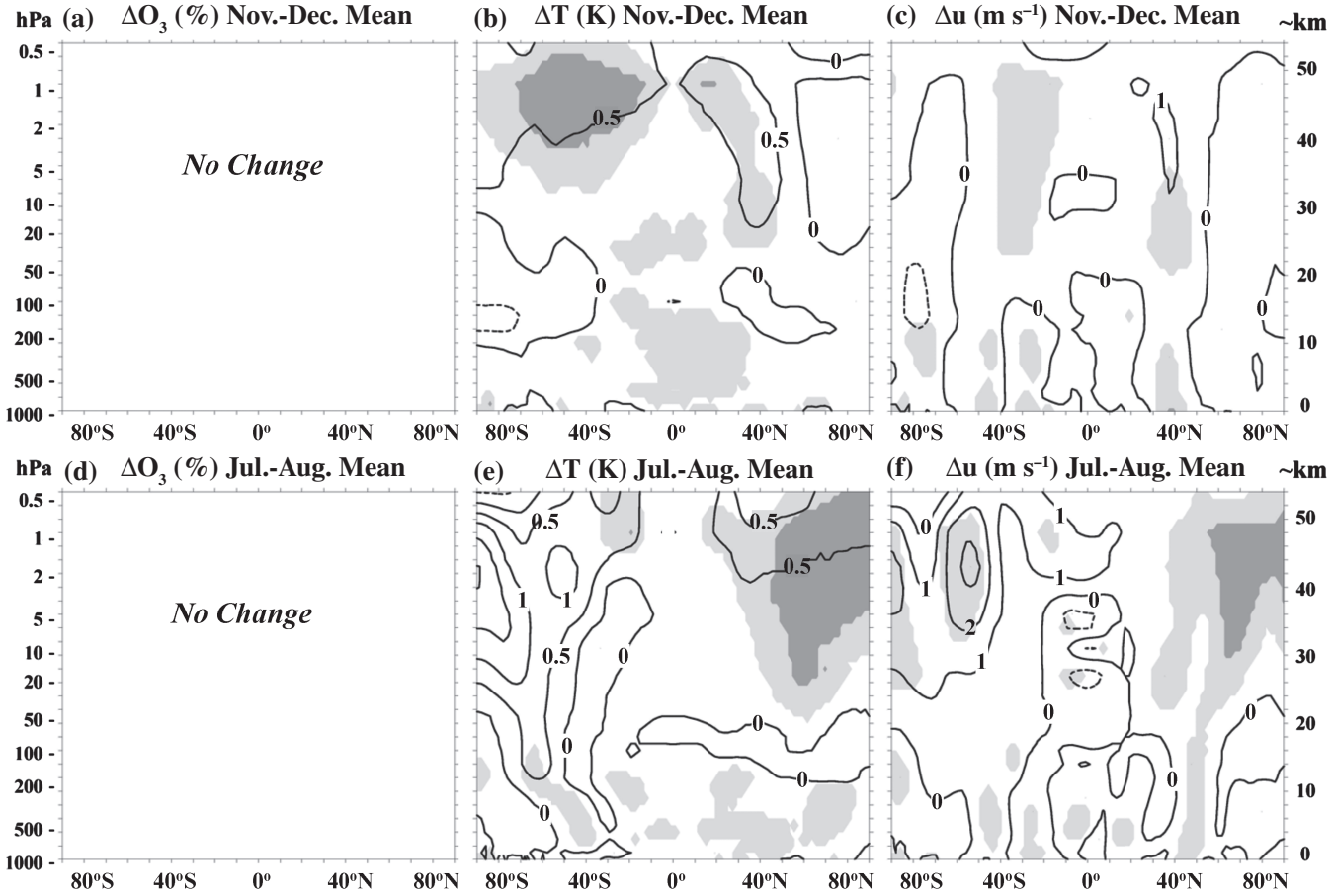

Figure 8. Solar cycle change (max–min) in zonal mean temperature and zonal wind during (a)–(c) early northern winter and (d)–(f) middle southern winter for the MIROCESM model (mean of three ensemble members) over the 1979–2005 period. This model used a prescribed ozone database which did not include a representation of the solar cycle. The contour interval is 0.5 K for temperature, and 1 m s^{-1} for zonal wind.

the interactive chemistry module. It differs from other high-top CMIP-5 models without interactive chemistry in that the ozone variation which was prescribed for this model did not include a representation of the solar cycle (Watanabe *et al.*, 2011). However, like the other CMIP-5 models, this model did impose a solar cycle variation of SSI (the NRL SSI). The model temperature and zonal wind responses therefore provide an interesting test of whether a realistic 11-year ozone variation in the upper stratosphere is important for producing a realistic thermal and dynamical response in winter. Figure 8 shows the ozone, temperature, and zonal wind changes from solar minimum to maximum during early northern winter and middle southern winter in the same format as Figure 7. (These averages were calculated from the ensemble mean monthly temperature and zonal wind solar regression coefficients plotted in Figures S28 and S29.) It is evident that this model produces no significant solar-induced latitudinal gradient in the temperature response and no corresponding positive zonal wind anomalies similar to those seen in Figure 7, even though a solar cycle SSI variation (but no accompanying ozone variation) was imposed. It is also interesting to note that there is no significant 11-year response of lower-stratospheric temperature in this model whereas there was at least a weak lower-stratospheric 11-year temperature response for the MIROC-ESM-CHEM model (Figure 2(b)).

Next, consider the three interactive models of Table 1 which did not produce a substantial upper-stratospheric ozone response and produced a relatively weak upper-stratospheric temperature response (GFDL-CM3, GISS-E2-H, and GISS-E2-R). Averaging together the ensemble and zonal mean ozone, temperature, and zonal wind responses during November–December and July–August for these three models yields the mean responses shown in Figure 9. Again, no significant latitudinal temperature response gradients and no significant zonal wind anomalies are produced by these models.

Next, consider the three interactive models of Table 1 which did produce a substantial upper-stratospheric ozone and temperature response (CESM1-WACCM, MIROC-ESM-CHEM, and MRI-ESM1). Averaging together the ensemble and zonal mean ozone, temperature, and zonal wind responses during the same time periods for these three models yields the mean responses shown in Figure 10. For these models, a mean negative latitudinal ozone gradient is obtained centred on latitudes ~70°N in November–December and 70°S in July–August. Accompanying temperature gradients with zero lines centred on about 60° in both hemispheres are obtained. Corresponding positive zonal wind anomalies with amplitudes of ~3 m s^{-1} in November–December centred at ~60°N and ~8 m s^{-1} in July–August centred near 45°S are obtained, although only the SH one is marginally significant. The structure of the SH wind signal is similar to that estimated from observations in that a weaker negative wind anomaly is present at higher latitudes. However, the mean amplitudes in both hemispheres are weaker by at least a factor of 2 than those estimated from the ERA-Interim data in Figure 7.

Lastly, Figure 11 shows a similar plot for the interactive model which produced the strongest and most significant 11-year response of upper-stratospheric ozone, the MRI-ESM1 model (Figures 1(c) and 2(c)). Only one historical simulation was completed for this model, so there is no guarantee that the results are representative of those for an ensemble mean. Nevertheless, we show them to illustrate that a larger response in the NH is possible in at least some simulations. As seen in Figure 11, the upper-stratospheric zonal wind anomaly is marginally significant with an amplitude of ~6 m s^{-1} and is centred near 50°N close to the stratopause. For comparison, the corresponding observational zonal wind anomaly has an amplitude of ~7 m s^{-1} and is centred near 30°N (Figure 5(c)). The model positive zonal wind anomaly in the SH in July–August is formally significant with a peak amplitude of 8 m s^{-1} near 2 hPa, which compares to a marginally

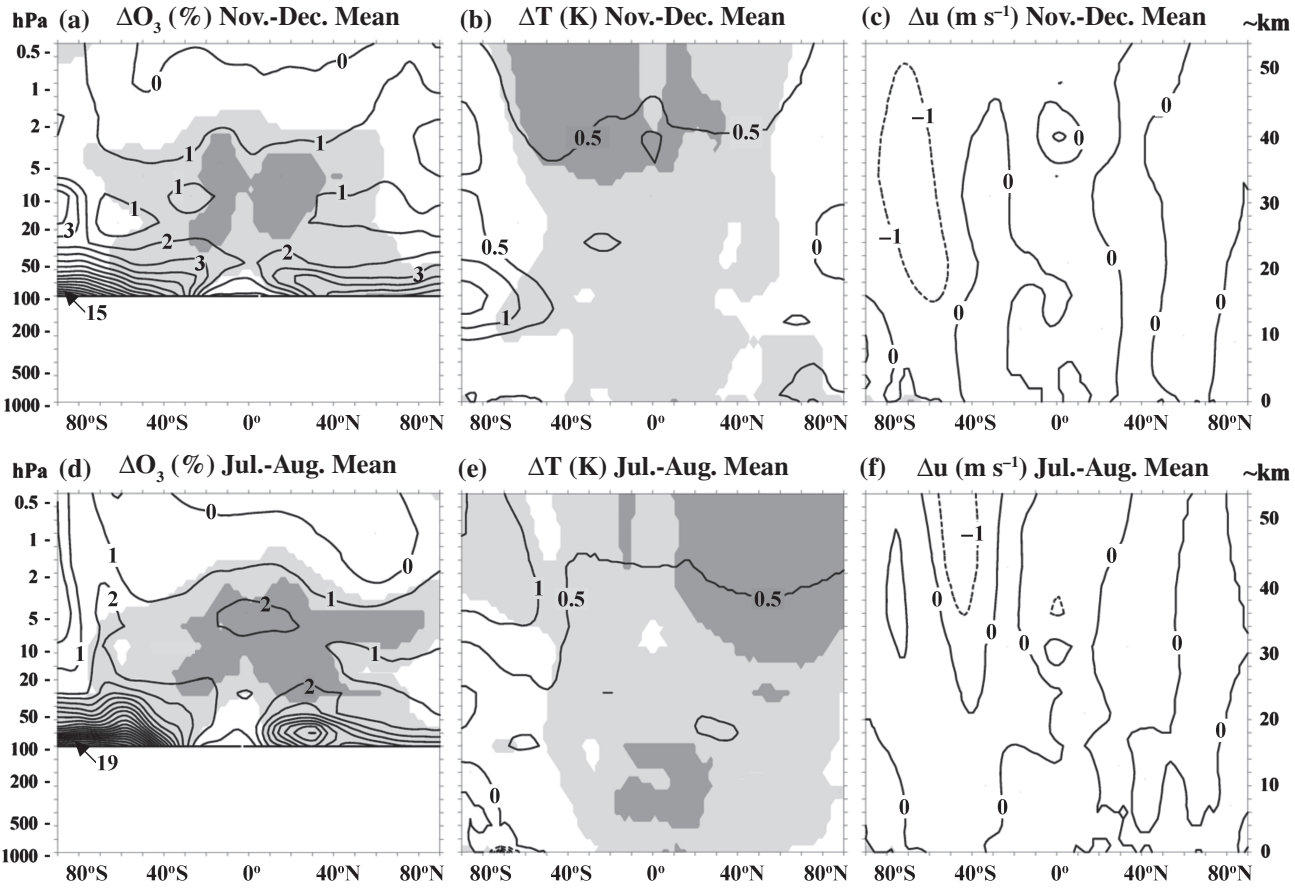

Figure 9. Mean solar cycle change (max−min) in zonal mean ozone, temperature, and zonal wind during (a)–(c) early northern winter and (d)–(f) middle southern winter for the three interactive chemistry models with relatively weak upper stratospheric ozone responses (GFDL-CM3, GISS-E2-H, and GISS-E2-R). The contour interval is 1% for ozone, 0.5 K for temperature, and 1 m s^{-1} for zonal wind.

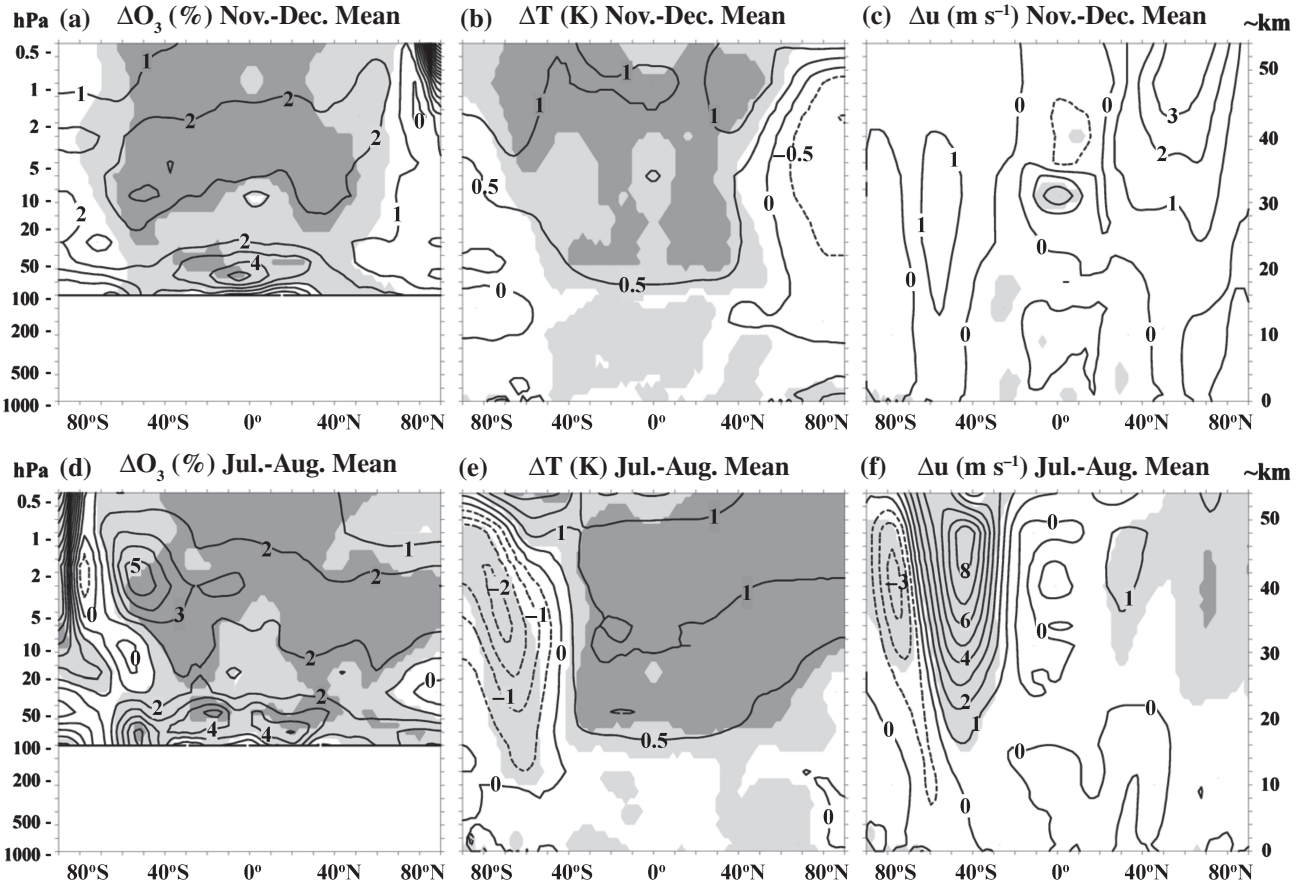

Figure 10. As Figure 9, but for the three interactive chemistry models with relatively strong upper-stratospheric ozone responses (CESM1-WACCM, MIROC-ESM-CHEM, and MRI-ESM1).

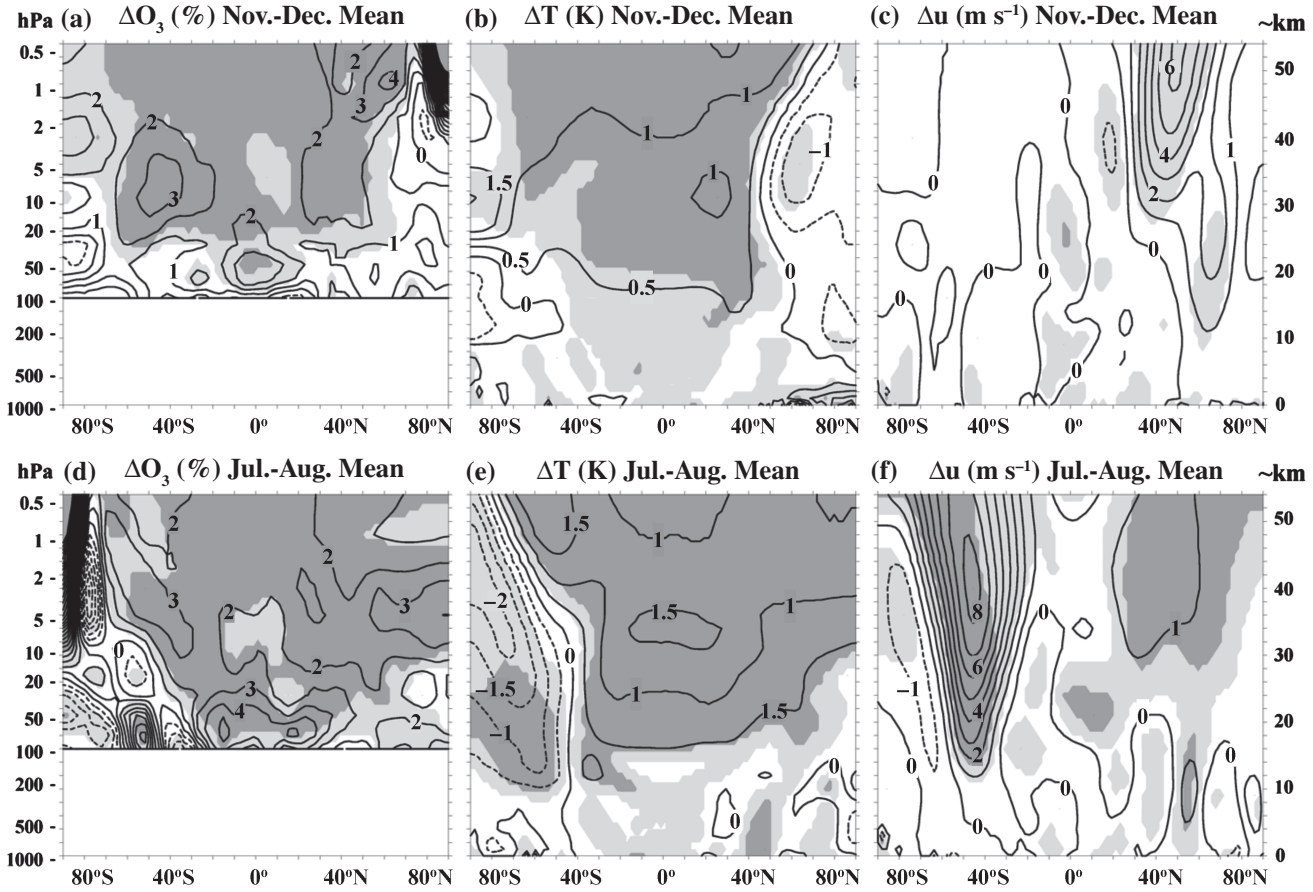

Figure 11. As Figures 9 and 10, but for the single MRI-ESM1 simulation over the 1979–2005 period.

significant anomaly derived from the ERA data with a peak amplitude of ∼13 m s^{-1} near the stratopause.

However, it should be noted that the large negative zonal wind response found in reanalysis data in February (section 3.3) is not simulated by any of the six models examined here.

4. Summary and discussion

A prerequisite for a successful model simulation of the top-down component of solar-induced climate change is that the model should produce an upper-stratospheric response of ozone, temperature, and zonal wind to 11-year solar forcing which agrees at least to first order with available observations (Kodera and Kuroda, 2002; Matthes *et al.*, 2006; Yukimoto and Kodera, 2007; Hood *et al.*, 2013). Since continuous global satellite measurements of stratospheric ozone and temperature began in 1979 and since the CMIP-5 model simulations cover the period up to 2005, this study has focused on the 1979–2005 period for detailed comparisons of solar signals in CMIP-5 models with available observations. Only the six models with high tops and interactive ozone chemistry were considered (Table 1). The Mg II solar UV index, derived from satellite SSI data, was adopted as the solar predictor or basis function in the MLR analysis (rather than TSI as done in Article 1) because it is available for this particular time period and produces larger and more statistically significant solar regression coefficients in stratospheric ozone data (e.g. Figure S12).

In section 2.5, it was found that three of the six models (CESM1-WACCM, MIROC-ESM-CHEM, and MRI-ESM1) produce substantial solar-induced responses of ozone and temperature in the upper stratosphere (Figures 1 and 2). This result was based on MLR analyses over 1979–2005 of four ensemble members for CESM1-WACCM, one member each for MIROC-ESM-CHEM and MRI-ESM1, and five members each for GFDL-CM3, GISS-E2-H, and GISS-E2-R. As found in sections 3.1 and 3.2, the observationally estimated annually averaged monthly ozone and temperature solar regression coefficients for the period after 1979 (Figures 3–6) compare favourably with the corresponding coefficients for CESM1-WACCM, MIROC-ESM-CHEM, and MRI-ESM1 in the upper stratosphere, especially when uncertainties in the observational estimates are taken into account. The remaining three models (GFDL-CM3, GISS-E2-H, and GISS-E2-R) yield much weaker upper-stratospheric responses which are difficult to reconcile with available observations. However, the latter three models do, in effect, provide a valuable baseline or set of control runs against which results for the three models with a substantial upper-stratospheric response can be compared.

As discussed in section 2.2, there are some significant differences in the radiation and photolysis codes for the six models which could potentially explain why only three of the models produce substantial 11-year upper-stratospheric ozone variations which agree with observational estimates. In the case of the GFDL-CM3 model, which produced the weakest 11-year ozone variation at most altitudes in the stratosphere, a coding error resulted in no time-varying solar flux for the chemistry code and therefore no photochemical ozone response. In the case of the two GISS-E2 models, the weak 11-year upper-stratospheric ozone variation could potentially be caused by omissions of O_2 absorption in the radiation code and the SRB contribution to O_2 dissociation in the photolysis rate code. The three models with substantial upper-stratospheric ozone variations have fewer issues overall, although WACCM also omits the contribution of O_2 absorption in the UV to radiative heating below 65 km and MIROC-ESM-CHEM omits water vapour photolysis. These deficiencies could potentially lead to some slight overestimation of the upper-stratospheric ozone response. The MRI-ESM1 model has no obvious omissions which would affect the solar-induced ozone variation in the upper stratosphere.

As also discussed extensively in sections 2.6 and 3.2, the 11-year response of lower-stratospheric ozone and temperature extracted by MLR in many of the six models considered here is probably

influenced by aliasing from the El Chichòn and Pinatubo volcanic aerosol injection events (Chiodo *et al.*, 2014). However, the extent of the aliasing appears to vary from model to model with results for some models (e.g. CESM1-WACCM) being strongly affected while those for others (e.g. MIROC-ESM-CHEM) are not very affected. Thus, the extent to which observational estimates of the lower-stratospheric response (which unfortunately are only available after 1979) are also affected by such aliasing is difficult to quantify based on the model simulations examined here. At least one model (MIROC-ESM-CHEM) simulates an 11-year ozone and temperature response in the lower stratosphere during a period (1955–1981) when there were no major volcanic aerosol injection events.

As found in section 3.3, in agreement with previous studies, the observationally estimated zonal wind response to 11-year solar forcing, although only marginally significant, has a maximum positive amplitude during NH early winter (November and December) and during SH middle winter (July and August). These zonal wind anomalies are accompanied by negative latitudinal gradients in the ozone and temperature responses during the same months in both winter hemispheres (Figure 7). Therefore, in section 3.4, a more detailed comparison of the ozone, temperature, and zonal wind responses from the six selected high-top models with the observationally estimated responses was carried out. It was first found (Figure 8) that three simulations using a version of MIROC-ESM-CHEM with no interactive chemistry and no representation of the solar cycle in its prescribed ozone variation produce no significant negative latitudinal temperature gradients or positive zonal wind anomalies in either winter hemisphere, even though a solar cycle variation of SSI (the NRL SSI model) was imposed in the model. This shows that such a model with no significant 11-year stratospheric ozone variation and a conservative SSI variation is not able to produce a realistic upper-stratospheric seasonal response. The three interactive chemistry models which did not produce a significant annually averaged response of upper-stratospheric ozone and only a weak temperature response also yielded no significant seasonal response in either hemisphere (Figure 9). The three interactive models which did produce annually averaged ozone and upper stratospheric responses agreeing to first order with observational constraints yielded a stronger combined upper-stratospheric seasonal response in both hemispheres, especially in the SH in July and August (Figure 10). The multi-model mean zonal wind response for these three models in November and December has an amplitude of only 3 m s^{-1} and is not statistically significant. But some simulations using these three models do produce a relatively strong zonal wind response during northern early winter which is consistent with observational estimates. In particular, the single MRI-ESM1 model simulation produces a mean zonal wind anomaly of $\sim$8 m s^{-1} during November and December (Figure 11). Several of the CESM1-WACCM simulations also produced a large positive wind anomaly during this season, although the ensemble mean amplitude was much weaker. Further simulations using the MRI-ESM1 model are needed to test whether the stronger northern winter zonal wind anomalies are a robust feature of this model for a conservative SSI variation.

The model ozone and temperature response gradients and the corresponding zonal wind anomalies of Figures 10 and 11 occur at somewhat higher latitudes than those estimated from observations (Figure 7). This difference has also been noted previously by Kodera *et al.* (2003) and may be related to an overall tendency for GCMs to simulate a polar night jet that is centred at a somewhat higher latitude than is observed. Kodera *et al.* (2003) have also argued that the inability of GCMs to produce an amplitude of the solar-induced polar night jet oscillation that is as large as estimated from observations is related to a failure to realistically produce interannual variability in the polar night jet amplitude. The treatments of dynamical processes for the six models considered here, including gravity wave parametrizations which are important for accurately simulating upper-stratospheric winds, are described in detail in the references listed in Table 1. None of the models have obvious deficiencies in this regard. However, the weaker and equatorward-shifted polar night jets for the two GISS models (section 2.3 and Figures S4 and S5) could reflect an increased influence of small-scale gravity waves on the circulation for this model. Their structure is similar to that obtained for polar night jets in the University of Illinois at Urbana-Champaign (UIUC) model when overly strong gravity wave drag was applied (Figure 5 of Yang *et al.*, 2000). The weaker amplitudes could also be related to the relatively low tops of the two GISS models ($\sim$66 km; Table 1). Finally, the overestimation of the SH polar night jet amplitude by CESM1-WACCM (section 2.3 and Figure S5) is likely related to a known SH cold pole bias for this model. The latter suggests a need for adjustments in the treatments of either planetary wave forcing or gravity waves. Possible approaches are currently being investigated by the WACCM team.

The negative latitudinal ozone response gradients in the winter high-latitude upper stratosphere that are found in both observations (Figure 7) and model simulations (e.g. Figures 10, 11 and S2(k)) are too strong to be due to the decrease with increasing latitude of the solar UV-induced ozone production rate. Instead, they are probably dynamical in origin since they are associated with positive zonal wind anomalies. It is unlikely that direct dynamical transport of ozone itself plays a role because the ozone chemical lifetime in the upper stratosphere is much shorter than dynamical time-scales. Rather it is more likely that ozone is responding photochemically to dynamically induced changes in temperature and/or other minor species concentrations which affect the ozone balance. The temperature changes seen in both observations and models have the same sign as the ozone changes, which is inconsistent with temperature feedback effects on ozone photochemistry (temperature increases alone result in ozone decreases, and vice versa in the upper stratosphere). Therefore, dynamically induced changes in minor species concentrations which are important for ozone catalytic losses may be implicated. For example, odd nitrogen has a photochemical lifetime near the stratopause ($\sim$1 month) which is much longer than dynamical time-scales (e.g. Brasseur and Solomon, 2005). Hence, a transport-induced increase in the latitudinal gradient of odd nitrogen in the upper stratosphere under solar maximum conditions would contribute to the negative latitudinal gradient in the ozone response for both models and observations. More detailed diagnostic analyses of the CMIP-5 models by the individual modelling groups is needed to test whether this process or others are involved.

Regardless of the exact origin of the negative latitudinal ozone response gradients, it is clear that they would assist in amplifying the zonal wind response. A strong negative latitudinal ozone gradient will radiatively enhance the negative latitudinal temperature gradient, which, by thermal wind balance, would amplify the zonal wind anomaly. This could therefore represent a positive feedback mechanism for producing a stronger upper-stratospheric dynamical response than expected for models that impose a conservative 11-year SSI variation. In any case, although further work is needed to assess models with prescribed ozone, the results of this analysis show that high-top models with interactive ozone chemistry that simulate substantial responses of ozone and temperature in the upper stratosphere are capable of producing a strong upper-stratospheric dynamical response. Such a dynamical response can, in turn, lead to significant troposphere–ocean signals in coupled models via the top-down mechanism (e.g. Yukimoto and Kodera, 2007).

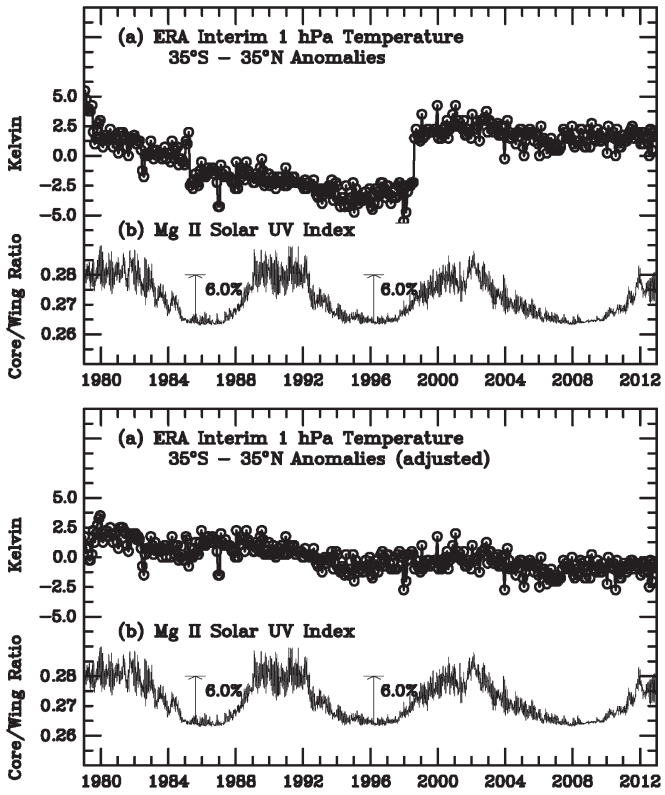

Figure A1. Top panel: (a) Area-weighted average over low latitudes of the ERA-Interim 1 hPa monthly temperature anomalies (deviations from long-term monthly means) and (b) the Mg II core-to-wing ratio solar UV index. Bottom Panel: as top panel but after offset adjustments are applied to the data (see text).

Appendix

ERA-Interim Temperature Adjustments

In this appendix, evidence for artificial offsets (step changes) in zonally averaged ERA-Interim temperature data in the upper stratosphere (5 hPa and above) is discussed and an empirical procedure is applied to adjust the data to minimize the offsets. The data were obtained at levels ranging from 1000 to 1 hPa (the highest level available for public access) from the European Centre for Medium-Range Weather Forecasts (http://apps.ecmwf.int/datasets; accessed 26 March 2015).

The top panel of Figure A1 compares deseasonalized anomalies (deviations from the long-term monthly means) of ERA-Interim temperature data at the highest available level (1 hPa) averaged over low latitudes (35°S to 35°N) to the Mg II solar UV index over the 1979–2012 period. Large offsets occur at several points in the time series which are apparently related to major changes in satellite instrumentation and/or changes in the reanalysis procedure. The largest single offset between July and August of 1998 closely follows the launch of the first Advanced Microwave Sounding Unit (AMSU) on the NOAA 15 satellite in May of that year. The AMSU was an improvement over the Microwave Sounding Unit (MSU), which began observations together with the SSU on TIROS-N in 1978. Other smaller offsets appear to occur between June and July of 1979 and between February and April of 1985. Offset errors of this type are clearly found in the data only at the 1, 2, and 5 hPa levels. McLandress *et al.* (2014) provide further discussion of these offset errors in the ERA Interim data and methods for minimizing them.

In order to estimate the magnitude of offset errors such as those in the top panel of Figure A1, a simple average of the low-latitude temperature anomalies was calculated in a 12-month window on either side of the offsets (except for the 1979 offset for which only 6 months were available to calculate the first average). The offset errors estimated from the differences between these two averages are:

1 hPa: 1979 −4.33 K; 1985 −1.87 K; 1998 +4.94 K;
2 hPa: 1979 −3.16 K; 1985 −1.38 K; 1998 +2.25 K;
5 hPa: 1998 −2.14 K.

Assuming that the offset errors estimated at low latitudes apply approximately to all latitudes, an adjusted monthly ERA-Interim dataset was constructed in which these estimated errors were minimized. The bottom panel of Figure A1 compares low-latitude temperature anomalies calculated from the adjusted data at 1 hPa to the Mg II UV index. As can be seen, the adjusted anomalies at this level exhibit a quasi-decadal variation that is roughly in phase with the solar cycle.

To test to what extent the offset errors may influence solar temperature regression coefficients derived from the ERA-Interim data, the MLR model (Eq. (1)) was applied separately to the unadjusted and adjusted data. It was found that the overall spatial structure of the solar regression coefficients was surprisingly similar for the two datasets, apparently due to the ability of the MLR method to identify solar-correlated decadal variations between the offset locations. However, the amplitudes of the solar temperature regression coefficients near the stratopause are increased by about 50% when using the unadjusted dataset rather than the adjusted dataset. Most of this increase is due to the fact that the large positive offset error in 1998 near 1 hPa occurs during a rising phase of the solar cycle, as seen in the top panel of Figure A1. Hence, the adjusted data provide a better estimate for the true amplitude of the solar-induced temperature response near the stratopause.

Supporting information

The following supporting information is available as part of the online article:

Figure S1. Observation-based annual mean ozone, annual mean temperature, December mean zonal wind, and July mean zonal wind (see text for a description of the datasets). The contour intervals are 1 ppmv for ozone, 5 K for temperature, and 5 m s^{-1} for zonal wind.

Figure S2. Annual and long-term zonal mean model ozone volume mixing ratio (ppmv) for each of the CMIP-5 models considered here. The contour interval is 1 ppmv.

Figure S3. As Figure S2 but for the annual and long-term zonal mean model temperature. The contour interval is 5 K.

Figure S4. As Figure S2 but for the long-term zonal mean model zonal winds for the month of December. The contour interval is 5 m s^{-1}.

Figure S5. As Figure S2 but for the long-term zonal mean model zonal winds for the month of July. The contour interval is 5 m s^{-1}.

Figure S6. Ensemble, monthly, and zonal mean ozone change (max−min) for the four CESM1-WACCM simulations over the 1979–2005 period (see text). Dark (light) shading indicates statistical significance at the 2 (1) sigma level. The contour interval is 1%.

Figure S7. As Figure S6 but for the single MIROC-ESM-CHEM simulation over the 1979–2005 period.

Figure S8. As Figure S6 but for the single MRI-ESM1 simulation over the 1979–2005 period.

Figure S9. As Figure S6 but for the five GFDL-CM3 simulations over the 1979–2005 period.

Figure S10. As Figure S6 but for the five GISS-E2-H simulations over the 1979–2005 period.

Figure S11. As Figure S6 but for the five GISS-E2-R simulations over the 1979–2005 period.

Figure S12. Annual, ensemble, and zonal mean ozone change (max−min) for the CESM1-WACCM model data over the 1979–2005 period calculated using a multiple linear regression statistical model for three different solar basis functions: (a) total solar irradiance, (b) the solar 10.7 cm radio flux, and (c) the solar Mg II core-to-wing ratio UV index.

Figure S13. Monthly zonal mean temperature change (max−min) for the four CESM1-WACCM simulations over the 1979–2005 period. Dark (light) shading indicates statistical significance at the 2 (1) sigma level. The contour interval is 0.5 K.

Figure S14. As Figure S13 but for the single MIROC-ESM-CHEM simulation over the 1979–2005 period.

Figure S15. As Figure S13 but for the single MRI-ESM1 simulation over the 1979–2005 period.

Figure S16. As Figure S13 but for the five GFDL-CM3 simulations over the 1979–2005 period.

Figure S17. As Figure S13 but for the five GISS-E2-H simulations over the 1979–2005 period.

Figure S18. As Figure S13 but for the five GISS-E2-R simulations over the 1979–2005 period.

Figure S19. Monthly zonal mean ozone change (max−min) for the Version 8 merged SBUV dataset over the 1979–2003 period. Dark (light) shading indicates statistical significance at the 2 (1) sigma level. The contour interval is 1%.

Figure S20. Monthly zonal mean temperature change (max−min) for the ERA-Interim dataset over the 1979–2012 period after adjustment to minimize offset errors in the upper stratosphere (see text). The contour interval is 0.5 K.

Figure S21. Monthly zonal mean zonal wind change (max−min) for the ERA-Interim dataset over the 1979–2012 period. The contour interval is 1 m s^{-1}.

Figure S22. Monthly zonal mean zonal wind change (max−min) for the four CESM1-WACCM simulations over the 1979–2005 period. Dark (light) shading indicates statistical significance at the 2 (1) sigma level. The contour interval is 1 m s^{-1}.

Figure S23. As Figure S22 but for the single MIROC-ESM-CHEM simulation over the 1979–2005 period.

Figure S24. As Figure S22 but for the single MRI-ESM1 simulation over the 1979–2005 period.

Figure S25. As Figure S22 but for the five GFDL-CM3 simulations over the 1979–2005 period.

Figure S26. As Figure S22 but for the five GISS-E2-H simulations over the 1979–2005 period.

Figure S27. As Figure S22 but for the five GISS-E2-R simulations over the 1979–2005 period.

Figure S28. Monthly zonal mean temperature change (max−min) for the three MIROC-ESM simulations over the 1979–2005 period. The contour interval is 0.5 K.

Figure S29. Monthly zonal mean zonal wind change (max−min) for the three MIROC-ESM simulations over the 1979–2005 period. The contour interval is 1 m s^{-1}.

Figure S30. As Figure 1 (annual mean max−min ozone response) but for the 1955–1981 period.

Figure S31. As Figure 2 (annual mean max−min temperature response) but for the 1955–1981 period.

Acknowledgements

The work reported here was directly motivated by the SPARC SOLARIS-HEPPA SolarMIP project. The authors thank all CMIP-5 modelling groups responsible for producing the simulations summarized in Table 1 and for providing their model data to the CMIP-5 archive. Special thanks go to Makato Deushi and Kiyotaka Shibata for clarifying the nature of the chemistry component of the MRI-ESM1 model and to Dan Marsh for helpful comments about the WACCM model. Comments and criticisms by the reviewers are also appreciated. Work at the University of Arizona was supported by grant 1251092 from the US National Science Foundation and by grant NNX14AD44G from the NASA Living With a Star program. Work at the University of Thessaloniki was supported by European Cooperation in Science and Technology (COST) Action ES1005 (Towards a more complete assessment of the impact of solar variability on the Earth's Climate –TOSCA). Work at the University of Oxford was supported by the UK Natural Environment Research Council as well as by TOSCA. Work at the World Radiation Center was supported by the Swiss National Science Foundation under grant CRSII2-147659 (FUPSOL II) and by the State Secretariat for Education, Research and Innovation of the Swiss Confederation under grant C11.01124 (SOVAC). Work at the GEOMAR Helmholtz Centre for Ocean Research in Kiel, Germany is partly supported within the Helmholtz University Young Investigators Group NATHAN funded by the Helmholtz Association through the President's Initiative and Networking Fund and by the GEOMAR.

References

Adachi Y, Yukimoto S, Deushi M, Obata A, Nakano H, Tanaka T, Hosaka M, Sakami T, Yoshimura H, Hirabara M, Shindo E, Tsujino H, Mizuta R, Yabu S, Koshiro T, Ose T, Kitoh A. 2013. Basic performance of a new Earth system model of the Meteorological Research Institute (MRI-ESM1). *Pap. Meteorol. Geophys.* **64**: 1–19, doi: 10.2467/mripapers.64.1.

Anderson J, Balaji V, Broccoli J, Cooke WF, Delworth TL, Dixon K, Donner L, Dunne K, Freidenreich SM, Garner S, Gudgel R, Gordon CT, Held IM, Hemler RS, Horowitz LW, Klein SA, Knutson TR, Kushner PJ, Langenhorst AR, Lau N-CH, Liang Z, Malyshev SL, Milly PCD, Nath MJ, Ploshay JJ, Ramaswamy V, Schwarzkopf MD, Shevliakova E, Sirutis JJ, Soden BJ, Stern WF, Thompson LA, Wilson RJ, Wittenberg AT, Wyman BL. 2004. The new GFDL global atmosphere and land model AM2-LM2: Evaluation with prescribed SST simulations. *J. Clim.* **17**: 4641–4673.

Austin J, Tourpali K, Rozanov E, Akiyoshi H, Bekki S, Bodeker G, Brühl C, Butchart N, Chipperfield M, Deushi M, Fomichev VI, Giorgetta MA, Gray LJ, Kodera K, Lott F, Manzini E, Marsh D, Matthes K, Nagashima T, Shibata K, Stolarski RS, Struthers H, Tian W. 2008. Coupled chemistry climate model simulations of the solar cycle in ozone and temperature. *J. Geophys. Res. Atmos.* **113**: D11306, doi: 10.1029/2007JD009391.

Bian H, Prather M. 2002. Fast-J2: Accurate simulations of photolysis in global climate models. *J. Atmos. Chem.* **41**: 281–296.

Brasseur GP, Solomon S. 2005. *Aeronomy of the Middle Atmosphere*. Springer: Berlin.

Briegleb B. 1992. Delta–Eddington approximation for solar radiation in the NCAR Community Climate Model. *J. Geophys. Res. Atmos.* **97**: 7603–7612.

Briegleb B, Light B. 2007. 'A Delta–Eddington multiple scattering parameterization for solar radiation in the sea ice component of the Community Climate System Model'. NCAR Technical Note TN-472+STR. National Center for Atmospheric Research: Boulder, CO.

Chabrillat S, Kockarts G. 1997. Simple parameterization of the absorption of the Lyman-alpha line. *Geophys. Res. Lett.* **24**: 2659–2662.

Chiodo G, Marsh DR, Garcia-Herrera R, Calvo N, Garcia JA. 2014. On the detection of the solar signal in the tropical stratosphere. *Atmos. Chem. Phys.* **14**: 5251–5269.

Chipperfield MP. 1999. Multiannual simulations with a three-dimensional chemical transport model. *J. Geophys. Res.* **104**: 1781–1805.

Chipperfield MP. 2006. New version of the TOMCAT/SLIMCAT offline chemical transport model: Intercomparison of stratospheric tracer experiments. *Q. J. R. Meteorol. Soc.* **132**: 1179–1203.

Cionni I, Eyring V, Lamarque JF, Randel WJ, Stevenson DS, Wu F, Bodeker GE, Shepherd TG, Shindell DT, Waugh DW. 2011. Ozone database in support of CMIP5 simulations: Results and corresponding radiative forcing. *Atmos. Chem. Phys.* **11**: 11267–11292.

Cochrane D, Orcutt DH. 1949. Application of least squares regression to relationships containing autocorrelated error terms. *J. Am. Stat. Assoc.* **44**: 32–61.

Crooks SA, Gray LJ. 2005. Characterization of the 11-year solar signal using a multiple regression analysis of the ERA-40 dataset. *J. Clim.* **18**: 996–1015.

Dee DP, Uppala SM, Simmons AJ, Berrisford P, Poli P, Kobayashi S, Andrae U, Balmaseda MA, Balsamo G, Bauer P, Balmaseda MA, Balsamo G, Bauer P, Bechtold P, Beljaars ACM, van de Berg L, Bidlot J, Bormann N, Delsol C, Dragani R, Fuentes M, Geer AJ, Haimberger L, Healy SB, Hersbach H, Hólm EV, Isaksen L, Kållberg P, Köhler M, Matricardi M, McNally AP, Monge-Sanz BM, Morcrette J-J, Park B-K, Peubey C, de Rosnay P, Tavolato C, Thépaut J-N, Vitart F. 2011. The ERA-Interim reanalysis: Configuration and performance of the data assimilation system. *Q. J. R. Meteorol. Soc.* **137**: 553–597, doi: 10.1002/qj.828.

Deushi M, Shibata K. 2011. Development of an MRI Chemistry-Climate Model ver. 2 for the study of tropospheric and stratospheric chemistry. *Pap. Meteorol. Geophys.* **62**: 1–46.

Dhomse S, Chipperfield MP, Feng W, Haigh JD. 2011. Solar response in tropical stratospheric ozone: A 3-D chemical transport model study using ERA reanalyses. *Atmos. Chem. Phys.* **11**: 12773–12786.

Donner LJ, Wyman BL, Hemler RS, Horowitz LW, Ming Y, Zhao M, Golaz J-C, Ginoux P, Lin S-J, Schwarzkopf MD, Austin J, Alaka G, Cooke WF, Delworth TL, Freidenreich SM, Gordon CT, Griffies SM, Held IM, Hurlin WJ, Klein SA, Knutson TR, Langenhorst AR, Lee H-C, Lin Y, Magi BI, Malyshev SL, Milly PCD, Naik V, Nath MJ, Pincus R, Ploshay JJ, Ramaswamy V, Seman CJ, Shevliakova E, Sirutis JJ, Stern WF, Stouffer RJ, Wilson RJ,

Winton M, Wittenberg AT, Zeng F. 2011. The dynamical core, physical parameterizations, and basic simulation characteristics of the atmospheric component AM3 of the GFDL global coupled model CM3. *J. Clim.* **24**: 3484–3519.

Ermolli I, Matthes K, Dudok de Wit T, Krivova NA, Tourpali K, Weber M, Unruh YC, Gray LJ, Langematz U, Pilewskie P, Rozanov E, Schmutz W, Shapiro A, Solanki SK, Woods TN. 2013. Recent variability of the solar spectral irradiance and its impact on climate modeling. *Atmos. Chem. Phys.* **13**: 3945–3977, doi: 10.5194/acp-13-3945-2013.

Eyring V, Arblaster J, Cionni I, SedlÆcek J, Perlwitz J, Young PJ, Bekki S, Bergmann D, Cameron-Smith P, Collins WJ, Faluvegi G, Gottschaldt K-D, Horowitz LW, Kinnison DE, Lamarque J-F, Marsh DR, Saint-Martin D, Shindell DT, Sudo K, Szopa S, Watanabe S. 2013. Long-term ozone changes and associated climate impacts in CMIP5 simulations. *J. Geophys. Res. Atmos.* **118**: 5029–5060, doi: 10.1002/jgrd.50316.

Fioletov VE. 2009. Estimating the 27-day and 11-year solar cycle variations in tropical upper stratospheric ozone. *J. Geophys. Res.* **114**: D02302, doi: 10.1029/2008JD010499.

Fortuin JPF, Kelder H. 1998. An ozone climatology based on ozonesonde and satellite measurements. *J. Geophys. Res.* **103**: 31709–31734.

Frame THA, Gray LJ. 2010. The 11-yr solar cycle in ERA-40 data: An update to 2008. *J. Clim.* **23**: 2213–2222.

Friedenreich S, Ramaswamy V. 1999. A new multiple-band solar radiative parameterization for general circulation models. *J. Geophys. Res. Atmos.* **104**: 31389–31409.

Garny H, Bodeker GE, Dameris M. 2007. Trends and variability in stratospheric mixing: 1979–2005. *Atmos. Chem. Phys.* **7**: 5611–5624.

Gray LJ, Crooks S, Pascoe C, Sparrow S, Palmer M. 2004. Solar and QBO influences on the timing of stratospheric sudden warmings. *J. Atmos. Sci.* **61**: 2777–2796.

Gray LJ, Rumbold ST, Shine KP. 2009. Stratospheric temperature and radiative forcing response to 11-year solar cycle changes in irradiance and ozone. *J. Atmos. Sci.* **66**: 2402–2417.

Gray LJ, Beer J, Geller M, Haigh J, Lockwood M, Matthes K, Cubasch U, Fleitmann D, Harrison G, Hood L, Luterbacher J, Meehl GA, Shindell D, van Geel B, White W. 2010. Solar influences on climate. *Rev. Geophys.* **48**: RG4001, doi: 10.1029/2009RG000282.

Gray LJ, Scaife AA, Mitchell DM, Osprey S, Ineson S, Hardiman S, Butchart N, Knight J, Sutton R, Kodera K. 2013. A lagged response to the 11 year solar cycle in observed winter Atlantic/European weather patterns. *J. Geophys. Res.: Atmos.* **118**: 13405–13420.

Haigh JD. 1994. The role of stratospheric ozone in modulating the solar radiative forcing of climate. *Nature* **370**: 544–546.

Haigh JD. 2003. The effects of solar variability on the Earth's climate. *Philos. Trans. R. Soc.: Math. Phys. Eng. Sci.* **361**: 95–111.

Harder JW, Fontenla JM, Pilewski P, Richard EC, Woods TN. 2009. Trends in solar spectral irradiance variability in the visible and infrared. *Geophys. Res. Lett.* **36**: L07801, doi: 10.1029/2008GL036797.

Heath D, Schlesinger B. 1986. The Mg 280 nm doublet as a monitor of changes in solar ultraviolet irradiance. *J. Geophys. Res.* **91**: 8672–8682.

Hood LL. 1986. Coupled stratospheric ozone and temperature responses to short-term changes in solar ultraviolet flux: An analysis of Nimbus 7 SBUV and SAMS data. *J. Geophys. Res.* **91**: 5264–5276.

Hood LL, Soukharev BE. 2012. The lower-stratospheric response to 11-yr solar forcing: Coupling to the troposphere–ocean response. *J. Atmos. Sci.* **69**: 1841–1864.

Hood LL, Huang Z, Bougher SW. 1991. Mesospheric effects of solar ultraviolet variations: Further analysis of SME IR ozone and Nimbus 7 SAMS temperature data. *J. Geophys. Res.* **96**: 12989–13002.

Hood LL, Jirikowic J, McCormack JP. 1993. Quasi-decadal variability of the stratosphere: Influence of long-term solar ultraviolet variations. *J. Atmos. Sci.* **50**: 3941–3958.

Hood LL, Soukharev BE, McCormack JP. 2010. Decadal variability of the tropical stratosphere: Secondary influence of the El Niño-Southern Oscillation. *J. Geophys. Res. Atmos.* **115**: D11113, doi: 10.1029/2009JD012291.

Hood LL, Schimanke S, Spangehl T, Bal S, Cubasch U. 2013. The surface climate response to 11-yr solar forcing during northern winter: Observational analyses and comparisons with GCM simulations. *J. Clim.* **26**: 7489–7506.

Huang T, Walters S, Brasseur G, Hauglustaine D, Wu W, Chabrillat S, Xuexi T, Granier C, Smith A, Kockarts G. 1998. 'Description of SOCRATES –a chemical dynamical radiative two-dimensional model'. Technical Note NCAR/TN-440+EDD. NCAR: Boulder, CO, doi:10.5065/D6K0726C.

Keating GM, Nicholson JY III Young DF, Brasseur G, De Rudder A. 1987. Response of middle atmosphere to short-term solar ultraviolet variations. 1: Observations. *J. Geophys. Res.* **92**: 889–902.

Kodera K, Kuroda Y. 2002. Dynamical response to the solar cycle. *J. Geophys. Res.: Atmos.* **107**: 4749, doi: 10.1029/2002JD002224.

Kodera K, Yamazaki K. 1990. Long-term variation of upper stratospheric circulation in the Northern Hemisphere in December *J. Meteorol. Soc. Jpn.* **68**: 101–105.

Kodera K, Matthes K, Shibata K, Langematz U, Kuroda Y. 2003. Solar impact on the lower mesospheric subtropical jet: A comparative study with general circulation model simulations. *Geophys. Res. Lett.* **30**: 1315, doi: 10.1029/2002GL016124.

Kopp G, Rottman G, Rottman G. 2005. The total irradiance monitor (TIM): Science results. In *The Solar Radiation and Climate Experiment (SORCE)*, 129–139. Springer: Berlin.

Koppers G, Murtagh D. 1996. Model studies of the influence of O_2 photodissociation parameterisation in the Schumann–Runge bands on ozone related photolysis in the upper atmosphere. *Ann. Geophys.* **14**: 68–79.

Kramarova NA, Frith SM, Bhartia PK, McPeters RD, Taylor SL, Fisher BL, Labow GJ, DeLand MT. 2013. Validation of ozone monthly zonal mean profiles obtained from the version 8.6 Solar Backscatter Ultraviolet algorithm. *Atmos. Chem. Phys.* **13**: 6887–6905.

Kyrölä E, Laine M, Sofieva V, Tamminen J, Pälvärinta S-M, Tukiainen S, Zawodny J, Thomason L. 2013. Combined SAGE II –GOMOS ozone profile data set 1984–2011 and trend analysis of the vertical distribution of ozone. *Atmos. Chem. Phys.* **13**: 10645–10658.

Lacis A, Hansen J. 1974. A parameterization for the absorption of solar radiation in the Earth's atmosphere. *J. Atmos. Sci.* **31**: 118–133.

Lean J. 2000. A decadal solar effect in the evolution of the Sun's spectral irradiance since the Maunder Minimum. *Geophys. Res. Lett.* **27**: 2425–2428, doi: 10.1029/2000GL000043.

Lean J, DeLand M. 2012. How does the Sun's spectrum vary? *J. Clim.* **25**: 2555–2560.

Lean J, Beer J, Bradley R. 1995. Reconstruction of solar irradiance since 1610: Implications for climate change. *Geophys. Res. Lett.* **22**: 3195–3198, doi: 10.1029/2005GL025342.

Lee H, Smith AK. 2003. Simulation of the combined effects of solar cycle, quasi-biennial oscillation, and volcanic forcing on stratospheric ozone changes in recent decades. *J. Geophys. Res.: Atmos.* **108**: 4049, doi: 10.1029/2001JD001503.

McCormick MP, Zawodny J, Veiga R, Larsen J, Wang PH. 1989. An overview of SAGE I and II ozone measurements. *Planet. Space Sci.* **37**: 1567–1586.

Madronich S, Flocke S. 1998. The role of solar radiation in atmospheric chemistry. In *Handbook of Environmental Chemistry*, Boule P. (ed.): 1–26. Springer: Berlin.

McLandress C, Plummer DA, Shepherd TG. 2014. Technical Note: A simple procedure for removing temporal discontinuities in ERA-Interim upper-stratospheric temperatures for use in nudged chemistry–climate model simulations. *Atmos. Chem. Phys.* **14**: 1547–1555.

McPeters RD, Bhartia PK, Haffner D, Labow GJ, Flynn L. 2013. The v8.6 SBUV ozone data record: An overview. *J. Geophys. Res.: Atmos.* **118**: 8032–8039, doi: 10.1002/jgrd.50597.

Marsh DR, Garcia RR, Kinnison DE, Boville BA, Sassi F, Solomon SC, Matthes K. 2007. Modeling the whole atmosphere response to solar cycle changes in radiative and geomagnetic forcing. *J. Geophys. Res.: Atmos.* **112**: D23306, doi: 10.1029/2006JD008306.

Marsh DR, Mills MJ, Kinnison DE, LaMarque J-F, Calvo N, Polvani L. 2013. Climate change from 1850 to 2005 simulated in CESM1(WACCM). *J. Clim.* **26**: 7372–7391.

Matthes K, Kuroda Y, Kodera K, Langematz U. 2006. Transfer of the solar signal from the stratosphere to the troposphere: Northern winter. *J. Geophys. Res.: Atmos.* **111**: D06108, doi: 10.1029/2005JD006283.

Meehl GA, Arblaster JM, Matthes K, Sassi F, van Loon H. 2009. Amplifying the Pacific climate system response to a small 11-year solar cycle forcing. *Science* **325**: 1114–1118.

Minschwaner K, Siskind D. 1993. A new calculation of nitric oxide photolysis in the stratosphere, mesosphere, and lower thermosphere. *J. Geophys. Res. Atmos.* **98**: 20401–20412.

Mitchell DM, Misios S, Gray LJ, Tourpali K, Matthes K, Hood L, Schmidt H, Chiodo G, Thiéblemont R, Rozanov E, Krivolutsky A. 2014a. Solar signals in CMIP-5 simulations: The stratospheric pathway. *Q. J. R. Meteorol. Soc.*, doi: 10.1002/qj.2530.

Mitchell DM, Gray LJ, Fujiwara M, Hibino T, Anstey JA, Ebisuzaki W, Harada Y, Long C, Misios S, Stott P, Tan D. 2014b. Signatures of naturally induced variability in the atmosphere using multiple reanalysis datasets. *Q. J. R. Meteorol. Soc.* doi: 10.1002/qj.2492.

Randel WJ, Wu F. 2007. A stratospheric ozone profile data set for 1979–2005: Variability, trends, and comparisons with column ozone data. *J. Geophys. Res.: Atmos.* **112**: D06313, doi: 10.1029/2006JD007339.

Remsberg EE. 2008. On the response of Halogen Occultation Experiment (HALOE) stratospheric ozone and temperature to the 11-year solar cycle forcing. *J. Geophys. Res.* **113**: D22304, doi: 10.1029/2008JD010189.

Remsberg EE. 2014. Decadal-scale responses in middle and upper stratospheric ozone from SAGE II version 7 data. *Atmos. Chem. Phys.* **14**: 1039–1053.

Russell GL, Miller JR, Rind D. 1995. A coupled atmosphere–ocean model for transient climate change studies. *Atmos. Ocean* **33**: 683–730.

Sato M, Hansen J, McCormick J, Pollack J. 1993. Stratospheric aerosol optical depths, 1850–1990. *J. Geophys. Res.* **98**: 22987–22994.

Scaife AA, Ineson S, Knight JR, Gray LJ, Kodera K, Smith DM. 2013. A mechanism for lagged North Atlantic climate response to solar variability. *Geophys. Res. Lett.* **40**: 434–439, doi: 10.1002/grl.50099.

Schmidt GA, Kelley M, Nazarenko L, Ruedy R, Russell GL, Aleinov I, Bauer M, Bauer SE, Bhat MK, Bleck R, Canuto V, Chen Y-H, Cheng Y, Clune TL, Del Genio A, de Fainchtein R, Faluvegi G, Hansen JE, Healy RJ, Kiang NY, Koch D, Lacis AA, LeGrande AN, Lerner J, Lo KK, Matthews EE, Menon S, Miller RL, Oinas V, Oloso AO, Perlwitz JP, Puma MJ, Putman WM, Rind

D, Romanou A, Sato M, Shindell DT, Sun S, Syed RA, Tausnev N, Tsigaridis K, Unger N, Voulgarakis A, Yao M-S, Zhang J. 2014. Configuration and assessment of the GISS ModelE2 contributions to the CMIP5 archive. *J. Adv. Model. Earth Syst.* **6**: 141–184, doi: 10.1002/2013MS000265.

Sekiguchi M, Nakajima T. 2008. A k-distribution based radiation code and its computational optimization for an atmospheric general circulation model. *J. Quant. Spectrosc. Radiat. Transfer* **109**: 2779–2793.

Shapiro AV, Rozanov EV, Shapiro AI, Egorova TA, Harder J, Weber M, Smith AK, Schmutz W, Peter T. 2013. The role of the solar irradiance variability in the evolution of the middle atmosphere during 2004–2009. *J. Geophys. Res. Atmos.* **118**: 3781–3793, doi: 10.1002/jgrd.50208.

Shibata K, Deushi M, Sekiyama TT, Yoshimura H. 2005. Development of an MRI chemical transport model for the study of stratospheric chemistry. *Pap. Meteorol. Geophys.* **55**: 75–119.

Shindell DT, Pechony O, Voulgarakis Z, Faluvegi G, Nazarenko L, Lamarque J-F, Bowman K, Milly G, Kovari B, Ruedy R, Schmidt GA. 2013. Interactive ozone and methane chemistry in GISS-E2 historical and future climate simulations. *Atmos. Chem. Phys.* **13**: 2653–2689.

Solomon S, Portmann RW, Garcia RR, Thomason LW, Poole LR, McCormick MP. 1996. The role of aerosol variations in anthropogenic ozone depletion at northern midlatitudes. *J. Geophys. Res.: Atmos.* **101**: 6713–6727.

Soukharev BE, Hood L. 2006. Solar cycle variation of stratospheric ozone: Multiple regression analysis of long-term satellite data sets and comparisons with models. *J. Geophys. Res.: Atmos.* **111**: D20314, doi: 10.1029/2006JD007107.

SPARC-CCMVal. 2010. *SPARC Report on the Evaluation of Chemistry–Climate Models*, SPARC Report No. 5, WCRP-132, WMO/TD-No. 1526, Eyring V, Shepherd TG, Waugh DW. (eds.). University of Toronto: Ontario, Canada, http://www.sparc-climate.org/publications/sparc-reports/sparc-report-no5 (accessed 29 March 2015).

Sukhodolov T, Rozanov E, Shapiro AI, Anet J, Cagnazzo C, Peter T, Schmutz W. 2014. Evaluation of the ECHAM family radiation codes performance in the representation of the solar signal. *Geosci. Model Dev. Discuss.* **7**: 1337–1356.

Sun S, Bleck R. 2006. Multi-century simulations with the coupled GISS-HYCOM climate model: Control experiments. *Clim. Dyn.* **26**: 407–428.

Taylor KE, Stouffer RJ, Meehl GA. 2012. An overview of CMIP-5 and the experiment design. *Bull. Am. Meteorol. Soc.* **93**: 485–498.

Thompson DWJ, Wallace JM. 1998. The Arctic Oscillation signature in the wintertime geopotential height and temperature fields. *Geophys. Res. Lett.* **25**: 1297–1300.

Tiao G, Reinsel G, Xu D, Pedrick J, Zhu X, Miller A, DeLuisi J, Mateer C, Wuebbles D. 1990. Effects of autocorrelation and temporal sampling schemes on estimates of trend and spatial correlation. *J. Geophys. Res.: Atmos.* **95**: 20507–20517.

Viereck R, Puga L. 1999. The NOAA MG II core-to-wing solar index: Construction of a 20-year time series of chromospheric variability from multiple satellites. *J. Geophys. Res.: Atmos.* **104**: 9995–10005.

Wang YM, Lean J, Sheeley N Jr. 2005. Modeling the sun's magnetic field and irradiance since 1713. *Astrophys. J.* **625**: 522–538.

Watanabe S, Hajima T, Sudo K, Nagashima T, Takemura T, Okajima H, Nozawa T, Kawase H, Abe M, Yokohata T, Ise T, Sato H, Kato E, Takata K, Emori S, Kawamiya M. 2011. MIROC-ESM 2010: Model description and basic results of CMIP5-20c3m experiments. *Geosci. Model Dev.* **4**: 845–872, doi: 10.5194/gmd-4-845-2011.

WMO. 2007. 'Scientific assessment of ozone depletion: 2006'. Report 50. pubGlobal Ozone Research and Monitoring Project, World Meteorological Organization: Geneva, Switzerland.

Woods TN. 2012. Solar irradiance variability: Comparisons of observations over solar cycles 21–24. In *EGU General Assembly Conference Abstracts*, Abbasi A, Giesen N. (eds.), Vol. **14**: 1520. Copernicus: Göttingen, Germany.

Yang F, Schlesinger ME, Rozanov E. 2000. Description and performance of the UIUC 24-layer stratosphere/troposphere general circulation model. *J. Geophys. Res.* **105**: 17925–17954, doi: 10.1029/2000JD900049.

Yukimoto S, Kodera K. 2007. Annular modes forced from the stratosphere and interactions with the oceans. *J. Meteorol. Soc. Jpn.* **85**: 943–952.

Yukimoto S, Yoshimura H, Hosaka M, Sakami T, Tsujino H, Hirabara M, Takana TY, Deushi M, Obata A, Nakano H, Adachi Y, Shindo E, Yabu S, Ose T, Kitoh A. 2011. 'MRI earth system model version 1 (MRI-ESM1) –Model Description'. Technical Report No. 64. Meteorological Research Institute: Tsukuba City, Japan, doi: 10.11483/mritechrepo.64.

Yukimoto S, Adachi Y, Hosaka M, Sakami T, Youshimura H, Hirabara M, Tanaka T, Shindo S, Tsujino H, Deushi M, Mizuta R, Yabu S, Obata A, Nakano H, Koshiro T, Ose T, Kitoh A. 2012. A new global climate model of the Meteorological Research Institute: MRI-CGCM3 Model description and basic performance. *J. Meteorol. Soc. Jpn.* **90A**: 23–64, doi: 10.2151/jmsj.2012-A02.

